Geophysical Journal International

Geophys. J. Int. (2011) **186,** 118–136 doi: 10.1111/j.1365-246X.2011.05037.x

Inference on core surface flow from observations and 3-D dynamo modelling

Alexandre Fournier, Julien Aubert and Erwan Thébault

Institut de Physique du Globe de Paris, Sorbonne Paris Cité, Université Paris Diderot, INSU/CNRS (UMR 7154), F-75005 *Paris, France.*
E-mail: fournier@ipgp.fr

Accepted 2011 April 1. Received 2011 April 1; in original form 2010 September 15

SUMMARY

We show how a 3-D, self-consistent numerical model of the geodynamo can be used as the subjective prior information for the determination of Earth's core surface flows from the geomagnetic field and its secular variation. This is achieved by estimating those parts of the numerical model state vector hidden from the observations, through a standard Kalman filtering (or stochastic inverse) procedure, where the Kalman gain matrix is based on the multivariate statistics of the geodynamo model. To allow for a direct comparison with observations, the field variables entering these statistics are scaled following two of the scaling laws that have recently come to the fore in numerical dynamo modelling, which express the dependency of the secular variation timescale and the magnetic energy density on their respective control parameters. We perform test experiments with noisy synthetic data, showing good to excellent recovery of the hidden parts of the state vector. A geomagnetic field model parent to a candidate model to the 2010 release of IGRF is then used for a core surface flow estimation. The estimated flow confirms the presence of convective columns underneath America, whereas exhibiting a high level of equatorial symmetry. We suggest that the discrete state estimation problem considered here (in connection with the classical core flow problem) could be used generically as a means to assess the degree of geophysical realism of a given geodynamo model. More generally, this study opens the way to using scaling laws and multivariate statistics from numerical models in the broader context of geomagnetic data assimilation.

Key words: Inverse theory; Dynamo: theories and simulations; Rapid time variations; Core, outer core and inner core.

1 INTRODUCTION

Assuming that we have knowledge of the radial component of the magnetic induction B_r and of its rate-of-change $\partial_t B_r$ at the top of Earth's core, the so-called core flow problem consists of trying to estimate the flow $\boldsymbol{u}$ compatible with these observations, by using the radial component of the magnetic induction equation

$$\partial_t B_r = -\nabla_h \cdot (\boldsymbol{u}_h B_r) + \lambda r^{-1} \nabla^2 (r B_r), \tag{1}$$

in which $\nabla_h \cdot$ is the horizontal divergence operator, λ is the magnetic diffusivity of the fluid core, and $\boldsymbol{u}_h = (u_\phi, u_\theta)$, where u_ϕ and u_θ are the eastward and southward horizontal components of the flow near the surface of the core, respectively. (In the remainder of this paper, (r, θ, ϕ) will refer to the standard spherical coordinates.) This problem has been the focus of a long-standing interest for the past 45 yr (see the reviews by Bloxham & Jackson 1991; Holme 2007). It is of fundamental importance, for its solution throws light on the underlying geodynamo process, while providing insight on important geophysical phenomena, such as the interannual to decadal changes in the length-of-day (see, e.g. Jault *et al.* 1988; Jackson *et al.* 1993; Gillet *et al.* 2010a). In their pioneering paper, Roberts & Scott (1965) proposed to neglect the effect of magnetic diffusion in eq. (1), on the account of its negligible contribution to the large-scale secular variation, leading to the popular frozen-flux approximation. Despite this important simplification, it was soon demonstrated by Backus (1968) that this problem is non-unique, and that further *a priori* hypotheses concerning the nature of the flow $\boldsymbol{u}$ are needed, along with regularization, for the inversion to yield a stable solution with a moderate level of spatial complexity. Hypotheses concerning the dynamics of the flow have included steadiness (see, e.g. Gubbins 1982; Voorhies 1986), tangential geostrophy (see, e.g. Le Mouël 1984; Jackson 1997), toroidal flows (see, e.g. Whaler 1986), helical flows (Amit & Olson 2004) or quasi-geostrophy (Pais & Jault 2008; Gillet *et al.* 2009). The solutions obtained by these various authors are generally quite sensitive to the imposed level of regularization (see also Pais *et al.* 2004). Even though, many studies agree on the existence of a westward current below Africa and the South Atlantic, and on the presence of a cyclone underneath the Indian Ocean

and that of an anticyclone under North America. In addition, the solutions yield flows whose large scales display a rather high level of equatorial symmetry, and whose typical rms amplitude is close to 15 km yr^{-1}. Other, smaller-scale, features, which depend sensitively on the non-uniqueness reducing hypothesis applied and the model/data used for the inversion, are less well-established. In fact, the level of ambiguity in the estimated flows has paradoxically become stronger with the advent of satellite-based field models during the last decade. These models are characterized by smaller error bars than their predecessors, thereby allowing small-scale features of the flow to be sought (Hulot *et al.* 2002; Holme & Olsen 2006). Consequently, the limiting factor in the core flow problem error budget has moved towards the modelling side, away from the observational side. The largest contribution to this budget seems to have now become that of the unmodelled secular variation, resulting from the interaction of the field concealed by the crust with the large-scale flow (Eymin & Hulot 2005). Recent studies have looked at this issue in quite some detail, trying to account for the unmodelled secular variation in the most sensible way when estimating core flows. To that end, Pais & Jault (2008) and Gillet *et al.* (2009) tried for instance to describe statistically the unmodelled secular variation by means of iterative or ensemble techniques, while Lesur *et al.* (2010) considered the possibility of adding a dynamic constraint (that of frozen-flux) in their joint inversion for field and flow from satellite data.

In this context, the novelty of our study lies in the introduction in the core flow problem of a subjective prior based on a 3-D, convection-driven model of the dynamo. This prior is derived from the statistics of those field variables which effectively take part in eq. (1). In practice, these 2-D fields are extracted from the full simulation, and are the surficial signature of the underlying 3-D dynamo process. These fields are not used in the context of the core flow problem for the first time: resorting to numerical dynamo models, Rau *et al.* (2000) and Amit *et al.* (2007) studied how well the different hypotheses involved in the resolution of the core flow problem were satisfied, according to the self-consistent truths represented by the various dynamo models they considered. They solved the core flow problem using synthetic data from maps of B_r and $\dot{B}_r$ extracted from their simulations, and sought a flow $\boldsymbol{u}$ compatible with these data and a given set of *a priori* assumptions. Their main conclusions were that the frozen-flux condition was fairly well satisfied, and that any *a priori* assumption could lead to a decent recovery of the true dynamo flow, even if the truncation of the data could generate large and unwanted artefacts (the location of which depended on the nature of the flow hypothesis).

Here we follow a different approach. The question we ask is: what is the core surface flow compatible with a set of geomagnetic data (in this instance, a geomagnetic field model) and the dynamics of a 3-D dynamo model? The dynamics enter this inverse problem in the form of the first and second moments defining the prior information (the mean and covariances). As already stated, these moments are constructed from a free run of the dynamo model, by extracting the 2-D multivariate statistics needed to tackle the core flow problem from the complete set of 3-D statistics characterizing the dynamo run. These multivariate statistics reflect the variability of B_r and $\dot{B}_r$ (at the core–mantle boundary, CMB) and that of $\boldsymbol{u}_h$ at the top of the free stream, during the integration of the model.

The core flow we find is obtained from the application of the Kalman gain matrix, which is the best linear unbiased estimator (BLUE) based on the statistics characterizing our two sources of information, the data and the prior (see e.g. Wunsch 2006). Therefore, we do not solve eq. (1) directly, but produce an estimate of field and flow supposed to reflect the fact that the induction equation (in its 3-D form) is solved while integrating the dynamo model, and should therefore impact the statistics used to construct the Kalman gain.

This paper is organized as follows. We begin by describing the bases of our inverse method in Section 2. We then focus on the numerical model of the geodynamo we resort to, with an emphasis on the procedure we use for upscaling its output to the Earth, and on the way we build the statistics we need to address the core flow problem. We next test our methodology and its implementation in the context of synthetic data in Section 4, before dealing with a geomagnetic field model in Section 5 (a parent of a candidate to the latest release of the international geomagnetic reference field). A summary and a discussion finally follow in Section 6.

2 THE INVERSE PROBLEM

In this section, we provide the notations used throughout this paper and a description of the theoretical bases supporting our estimate of the core flow, based on the joint use of a numerical model of the geodynamo (our prior description of the state of the core), and of a geomagnetic field model at the CMB. The material that follows is rather standard; the interested reader will find it declined in a meteorological context in the seminal paper of Lorenc (1986), where the concept of a prior relying on a dynamic model was explicit. In the context of geomagnetic field modelling, and in the framework of stochastic inversion, Gubbins (1983) derived the same generic solution we shall come up with, considering various types of *a priori* constraints one could resort to when building a geomagnetic field model.

In the following, we will consider the static (instantaneous) problem consisting of estimating, at a given time, the optimal state of the core $\mathbf{x}$ compliant with the *a priori* information supplied by the numerical dynamo model and a set of observations $\mathbf{y}^o$, in that instance a geomagnetic field model at the CMB. The exact discrete forms of $\mathbf{x}$ and $\mathbf{y}^o$ will be provided in Sections 3.2, 4 and 5, respectively. For the time being, we assume that $\mathbf{x}$ and $\mathbf{y}^o$ are column vectors of size $N_\mathbf{x}$ and $N_{\mathbf{y}^o}$, respectively, containing complex-valued coefficients. In the following, a star $\star$ will indicate complex conjugation, a superscript T transposition, and a dagger † the conjunction of complex conjugation and transposition. The standard Hermitian product gives the measurement of the length of vectors (see, e.g. Arfken & Weber 1995). For instance, the length of the state vector, $l(\mathbf{x})$, is given by

$$l(\mathbf{x}) = \sqrt{\mathbf{x}\dagger\mathbf{x}}. \tag{2}$$

We introduce the probability density function $p\left(\mathbf{x}^t|\mathbf{y}^o\right)$ associated with the occurrence of the realization of the true state of the core $\mathbf{x}^t$ given the observation at hand $\mathbf{y}^o$. Our task is to find an optimal estimate $\widehat{\mathbf{x}}$ of the state of the core which will maximize this probability

density function (pdf). To proceed, we follow Lorenc (1986) and recall Bayes' theorem, which stipulates that the posterior probability of an event A occurring, given that an event B is known to have occurred, is proportional to the prior probability of A, multiplied by the probability of B occurring given that A is known to have occurred. Here the event A refers to the realization of $\mathbf{x} = \mathbf{x}^{\mathrm{t}}$ and event B refers to the set of observations being $\mathbf{y}^{\mathrm{o}}$. Consequently, introducing the corresponding two additional pdfs, we write

$$p(\mathbf{x}^{\mathrm{t}}|\mathbf{y}^{\mathrm{o}}) \propto p(\mathbf{y}^{\mathrm{o}}|\mathbf{x}^{\mathrm{t}})p(\mathbf{x}^{\mathrm{t}}). \tag{3}$$

The prior probability density function $p\left(\mathbf{x}^{\mathrm{t}}\right)$ encapsulates our knowledge of the core before observations are made and incorporated into the analysis. We describe it in terms of a deviation from a known background state $\mathbf{x}^{\mathrm{b}}$,

$$p(\mathbf{x}^{\mathrm{t}}) = p^{\mathrm{b}}(\mathbf{x} - \mathbf{x}^{\mathrm{b}}). \tag{4}$$

To proceed further, we need to specify the pdf p^{b}. A common and simplifying assumption is that p^{b} is a multidimensional Gaussian function, such that

$$p^{\mathrm{b}}(\mathbf{x} - \mathbf{x}^{\mathrm{b}}) \propto \exp\left[-\frac{1}{2}(\mathbf{x} - \mathbf{x}^{\mathrm{b}})^{\dagger}\mathbf{P}^{\mathrm{b}^{-1}}(\mathbf{x} - \mathbf{x}^{\mathrm{b}})\right]. \tag{5}$$

The $N_{\mathbf{x}} \times N_{\mathbf{x}}$ matrix $\mathbf{P}^{\mathrm{b}}$ possesses the property $\mathbf{P}^{\mathrm{b}^{\dagger}} = \mathbf{P}^{\mathrm{b}}$ (it is Hermitian) and is termed the background error covariance matrix. In a dynamic context, the prior information contained in that matrix should be constantly updated as the model evolves in model space and more information on the state of the system is supplied by the stream of observations (see, e.g. Fournier *et al.* 2010, and references therein). For a kinematic instantaneous problem such as the core flow problem, there is no need to worry about that issue. Still, a central concern remains the definition of a proper background state, and the approximation of the variability of the system by a Gaussian pdf. We will come back to these issues in the specific context of our numerical model of the geodynamo in Section 3.3.

We now introduce the (assumed linear) observation operator $\mathbf{H}$ which maps the model space onto the space of observations. Let us define the observation error $\boldsymbol{\epsilon}^{\mathrm{o}}$ as

$$\boldsymbol{\epsilon}^{\mathrm{o}} = \mathbf{H}\mathbf{x}^{\mathrm{t}} - \mathbf{y}^{\mathrm{o}}. \tag{6}$$

We assume again that the statistical properties of the observation error are Gaussian (and independent from that of the prior introduced above); this ought to be the case if the observations consist of geomagnetic field models derived in a least-squares sense, as considered in Section 5. We thus write

$$p(\mathbf{y}^{\mathrm{o}}|\mathbf{x}^{\mathrm{t}}) \propto \exp\left(-\frac{1}{2}\boldsymbol{\epsilon}^{\mathrm{o}\dagger}\mathbf{R}^{-1}\boldsymbol{\epsilon}^{\mathrm{o}}\right), \tag{7}$$

in which $\mathbf{R}$ is the $N_{\mathbf{y}^{\mathrm{o}}} \times N_{\mathbf{y}^{\mathrm{o}}}$ observation error covariance matrix, which is also Hermitian by construction.

Gathering the contributions of prior and observational pdfs in eq. (3), we see that our preferred estimate is the one minimizing the functional

$$J(\mathbf{x}) = \frac{1}{2}\left[(\mathbf{H}\mathbf{x} - \mathbf{y}^{\mathrm{o}})^{\dagger}\mathbf{R}^{-1}(\mathbf{H}\mathbf{x} - \mathbf{y}^{\mathrm{o}}) + (\mathbf{x} - \mathbf{x}^{\mathrm{b}})^{\dagger}\mathbf{P}^{\mathrm{b}^{-1}}(\mathbf{x} - \mathbf{x}^{\mathrm{b}})\right]. \tag{8}$$

We cast that minimization problem in terms of the incremental state vector $\delta\mathbf{x}$ defined as

$$\delta\mathbf{x} \equiv \mathbf{x} - \mathbf{x}^{\mathrm{b}}, \tag{9}$$

and find that the best estimate $\widehat{\delta\mathbf{x}}$ minimizing

$$J(\delta\mathbf{x}) = \frac{1}{2}\left[\left(\mathbf{H}\delta\mathbf{x} + \mathbf{H}\mathbf{x}^{\mathrm{b}} - \mathbf{y}^{\mathrm{o}}\right)^{\dagger}\mathbf{R}^{-1}\left(\mathbf{H}\delta\mathbf{x} + \mathbf{H}\mathbf{x}^{\mathrm{b}} - \mathbf{y}^{\mathrm{o}}\right) + \delta\mathbf{x}^{\dagger}\mathbf{P}^{\mathrm{b}^{-1}}\delta\mathbf{x}\right] \tag{10}$$

is defined by

$$\widehat{\delta\mathbf{x}} = [\mathbf{H}^{\dagger}\mathbf{R}^{-1}\mathbf{H} + \mathbf{P}^{\mathrm{b}^{-1}}]^{-1}\mathbf{H}^{\dagger}\mathbf{R}^{-1}\left(\mathbf{y}^{\mathrm{o}} - \mathbf{H}\mathbf{x}^{\mathrm{b}}\right) = \mathbf{K}\left(\mathbf{y}^{\mathrm{o}} - \mathbf{H}\mathbf{x}^{\mathrm{b}}\right). \tag{11}$$

This expression involves the so-called Kalman gain

$$\mathbf{K} \equiv [\mathbf{H}^{\dagger}\mathbf{R}^{-1}\mathbf{H} + \mathbf{P}^{\mathrm{b}^{-1}}]^{-1}\mathbf{H}^{\dagger}\mathbf{R}^{-1}, \tag{12}$$

which is ubiquitous in the data assimilation literature (see, e.g. Kalnay 2003), but appears generally under this equivalent form

$$\mathbf{K} = \mathbf{P}^{\mathrm{b}}\mathbf{H}^{\dagger}\left[\mathbf{H}\mathbf{P}^{\mathrm{b}}\mathbf{H}^{\dagger} + \mathbf{R}\right]^{-1}. \tag{13}$$

The main reason for using this latter formula (the equivalence of which is derived in Appendix A) is that the matrix $\mathbf{H}\,\mathbf{P}^{\mathrm{b}}\,\mathbf{H}^{\dagger} + \mathbf{R}$ that needs to be inverted has size $N_{\mathbf{y}^{\mathrm{o}}} \times N_{\mathbf{y}^{\mathrm{o}}}$, as opposed to $N_{\mathbf{x}} \times N_{\mathbf{x}}$ for $\mathbf{H}^{\dagger}\mathbf{R}^{-1}\,\mathbf{H} + \mathbf{P}^{\mathrm{b}^{-1}}$ in eq. (12) (which requires in addition three inversions in lieu of one). Eq. (13) is the one we shall resort to in this study, because the size of a geomagnetic field model is much smaller than that of the state vector ($N_{\mathbf{y}^{\mathrm{o}}} \ll N_{\mathbf{x}}$).

Having laid the framework for our discrete estimation problem, we now need to define more precisely how we construct each of its constituents.

3 THE NUMERICAL GEODYNAMO MODEL AS THE SOURCE OF PRIOR INFORMATION

In this section we describe the numerical model of the geodynamo which defines our prior information, with an emphasis on the nature of the state vector $\mathbf{x}$, on the background state $\mathbf{x}^{\mathrm{b}}$, and on the construction and structure of the matrix $\mathbf{P}^{\mathrm{b}}$. Some basic facts about the model we choose are recalled in Appendix B. Note in particular that the model is driven by chemical buoyancy, and that no-slip kinematic boundary conditions are employed. The model is characterized by four distinct non-dimensional parameters, the Ekman number E, Prandtl number Pr, magnetic Prandtl number Pm, and Rayleigh number Ra, whose definitions are recalled in Appendix B. The model has

$$(\mathrm{E}, \mathrm{Pr}, \mathrm{Pm}, \mathrm{Ra}) = (10^{-3}, 1, 4, 5.8\ 10^{-3}), \tag{14}$$

to compare with the approximate values for the Earth:

$$(\mathrm{E}, \mathrm{Pr}, \mathrm{Pm}, \mathrm{Ra}) \approx (10^{-14}, 10^{-2}, 10^{-5}, 10^{-13}). \tag{15}$$

Despite the relatively weak chemical forcing, the rather large value of the magnetic Prandtl number makes dynamo action possible, and the model has a magnetic Reynolds number Rm equal to 100.

After completion of an initial spin-up, the model has been integrated over a time window of width roughly equal to 54 viscous diffusion times (after application of the scaling procedure described below, this amounts to ∼240 000 yr). From this sequence, we extracted $N_e = 18\,000$ samples equally spaced in time to define our first and second-order statistical moments, $\mathbf{x}^{\mathrm{b}}$ and $\mathbf{P}^{\mathrm{b}}$, respectively. In order to focus on the core flow problem, we extracted 2-D features out of the fully 3-D numerical integration. Consequently, our samples only involve the field and its rate-of-change at the CMB, and the flow at the top of the free stream, the location of which we determined empirically following Rau *et al.* (2000).

3.1 Scaling

We begin by defining the procedure we chose to scale a generic non-dimensional model quantity $\underline{q}$ to its geophysical counterpart q. Of interest here are the scalings for time, velocity, and magnetic induction, since we wish ultimately to make direct comparisons between the secular variation of the numerical model and the geomagnetic secular variation. These scalings are based on the underlying assumption that the model and the Earth obey equally well a known scaling law predicting the value of q from the input control parameters (see, e.g. Christensen & Aubert 2006; Christensen 2010; Wicht *et al.* 2010). They should be interpreted as an attempt to compensate for the discrepancy between the values taken by some parameters in the numerical model and those expected for the Earth.

3.1.1 Time

Central to our scaling for time is the notion of instantaneous correlation time τ_l for a given spherical harmonic degree l, introduced by Hulot & Le Mouël (1994), and defined as

$$\tau_l(t) = \left[\frac{\sum_{m=0}^{l} g_{lm}^2(t) + h_{lm}^2(t)}{\sum_{m=0}^{l} \dot{g}_{lm}^2(t) + \dot{h}_{lm}^2(t)} \right]^{1/2}, \tag{16}$$

in which g_{lm} and h_{lm} are the usual Gauss coefficients of degree l and order m, and a dot denotes time derivative. In their analysis of numerical and laboratory dynamo models, Christensen & Tilgner (2004) define the timescale of secular variation as the square root of the ratio of the time-average of the same quantities

$$\overline{\tau}(l) = \left[\frac{\overline{\sum_{m=0}^{l} g_{lm}^2 + h_{lm}^2}}{\overline{\sum_{m=0}^{l} \dot{g}_{lm}^2 + \dot{h}_{lm}^2}} \right]^{1/2}, \tag{17}$$

in which the overbar denotes time-averaging. Christensen & Tilgner (2004) find that $\overline{\tau}(l)$ can be reasonably well approximated by

$$\overline{\tau}(l) = \frac{\tau_{\mathrm{sec}}}{l}, \tag{18}$$

in which τ_{sec} is the secular variation time constant. Christensen & Tilgner (2004) find that this dependence is clearer in their numerical database than in the geomagnetic record, most likely because the numerical time-series last effectively longer than the geomagnetic record (they usually span several magnetic diffusion times) ; see also the discussion in Holme & Olsen (2006) and further support for an inverse linear dependence of $\overline{\tau}(l)$ on l in Lhuillier *et al.* (2011). The approximation given by eq. (18) is also appropriate for the sequence we generated. Fig. 1 shows for illustration a collection of dimensionless instantaneous correlation times $\underline{\tau}(l)$ computed for 41 (out of the 18 000) samples roughly equally spaced in time (black curves, squares). Also shown in Fig. 1 are the dimensionless correlation times computed according to eq. (17) (red curve, diamonds), for which the averaged spectra were determined over the entire duration of the simulation (54 viscous diffusion times, see above). The least-squares fit to a law of the form given by eq. (18) (obtained by retaining spherical harmonic degrees $2 \leq l \leq 64$) is shown in blue. This trend will allow us to define the scaling/extrapolation of model time to geophysical time. Before doing so, we must still perform a consistency check, by proving that our particular dynamo model pertains to the generic class of models used by Christensen & Tilgner (2004), and is therefore amenable to extrapolation to the Earth. Such a check is given by the variation of τ_{sec} (normalized by the dipole diffusion time $\tau_{\mathrm{dip}} = \mathcal{L}^2/(\pi^2\lambda)$) to the magnetic Reynolds number Rm. According to Christensen & Tilgner (2004), and based on our

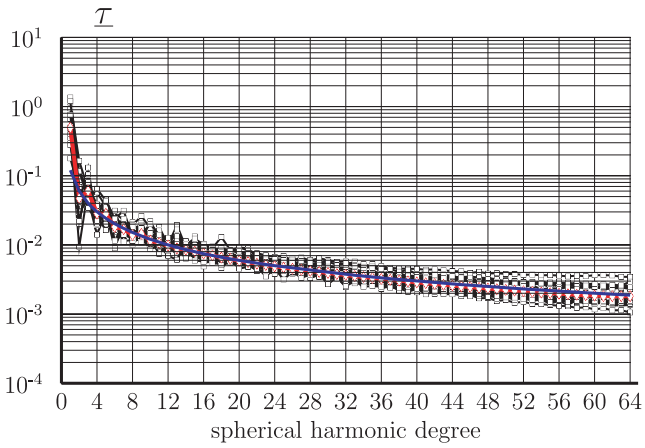

Figure 1. Non-dimensional instantaneous correlation times $\underline{\tau}$ as a function of spherical harmonic degree l, for 41 samples out of the 18 000 samples we extracted from the dynamo sequence (black curves, with squares). Red line (with diamonds): timescale of secular variation $\overline{\underline{\tau}}(l)$ (see text for details). Blue line: least-squares fit of the form $\overline{\underline{\tau}}(l) = \underline{\tau_{sec}}/l$.

scaling conventions, one should expect a dependency of the form

$$\frac{\tau_{\rm sec}}{\tau_{\rm dip}} \approx 33.2\,{\rm Rm}^{-1}. \tag{19}$$

In our case, we find for the left-hand side a value of 0.297. For our value of Rm (100, see above), it falls within 1σ of the general trend found by Christensen & Tilgner (2004), see their fig. 3(b), and bear in mind that using their scaling conventions, the left-hand side of eq. (19) becomes 0.194, and Rm goes up to 153. Our line of reasoning from here is straightforward: we scale the non-dimensional numerical time by a factor F_τ given by $F_\tau = \tau_{\rm sec}({\rm Earth})/\underline{\tau_{\rm sec}}({\rm model})$, the former taken to be 535 yr according to Christensen & Tilgner (2004), and the latter found by the least-squares fit yielding the blue curve in Fig. 1, as recommended by Lhuillier *et al.* (2011). After applying this factor, we find that the time window of the dynamo sequence used to construct our model statistics spans $T = 240\,270$ yr.

3.1.2 Velocity

Since we now know how to scale time, we simply scale velocity by a factor equal to $\mathcal{L}/F_\tau$, in which $\mathcal{L}$ is the length scale (the depth of the core). The typical rms surface flow speed resulting from this scaling is on the order of 12 km yr^{-1}.

3.1.3 Magnetic induction

We now follow a similar line of reasoning for the scaling of the amplitude of the magnetic field $\boldsymbol{B}$. Our first task is to check whether our model is compliant with the scaling law for the rms strength of the field $B_{\rm rms}$ given by Christensen & Aubert (2006) and Aubert *et al.* (2009), which is

$$\frac{B_{\rm rms}}{\sqrt{\rho\mu}\Omega\mathcal{L}} \propto f_{\rm Ohm}^{1/2}\left(\frac{p}{\rho\Omega^3\mathcal{L}^2}\right)^{0.34}, \tag{20}$$

where ρ is density, μ is the magnetic permeability, Ω is the angular velocity, p is the convective power density, and $f_{\rm Ohm}$ is the fraction of power dissipated through Ohmic losses. In the case of the Earth, this number is close to 1, whereas it is more variable in models which have significant viscous dissipation. That is the case for the model used in this study, which is characterized by $f_{\rm Ohm} = 0.378$, and, accordingly, by a ratio of the left-hand side to the right-hand side of eq. (20) equal to 1.31. This value is in line with the general trend depicted in the study of Aubert *et al.* (2009), see their fig. 4. Our fundamental rescaling assumption is then that the ratio of pointwise $\boldsymbol{B}$ to $B_{\rm rms}$ is a constant shared by the numerical model and the Earth. Therefore, extrapolating the magnetic field amplitude predicted by the model to the Earth amounts to multiplying its dimensionless value by a factor $F_B = B_{\rm rms}({\rm Earth})/\underline{B_{\rm rms}}({\rm model})$, taking $B_{\rm rms}({\rm Earth}) = 2.4$ mT if we follow the high-power scenario of Aubert *et al.* (2009).

In Fig. 2, we plot the CMB Mauersberger–Lowes spectra (Mauersberger 1956; Lowes 1974) of the field and secular variation, obtained after multiplying the dimensionless outputs of the simulation by factors F_B and F_B/F_τ, respectively. The field is characterized by a dominant dipole and a relatively low quadrupole. Fig. 2 (right-hand panel) emphasizes that the secular variation of our model is essentially generated in a 5–20 spherical harmonic degree band. At higher degrees, it decreases and reaches at $l = 64$ (the numerical truncation) a level similar to that of the dipole secular variation.

We finish that scaling section by noting that another scaling option for $\boldsymbol{B}$ has been followed by, for example, Kuang *et al.* (2009), who use a scaling factor F'_B given by $F'_B = g_1^0({\rm Earth})/\underline{g_1^0}({\rm model})$, in which g_1^0 is the Gauss coefficient for the axial dipole. Here, using the time average of $\underline{g_1^0}({\rm model})$, and the current value of g_1^0 (Earth), leads to a scaling factor $F'_B = 0.62\,F_B$, hence to an underestimation of the strength of the field. This other strategy has however the advantage of being based on a quantity, g_1^0 (Earth), very well known from observations.

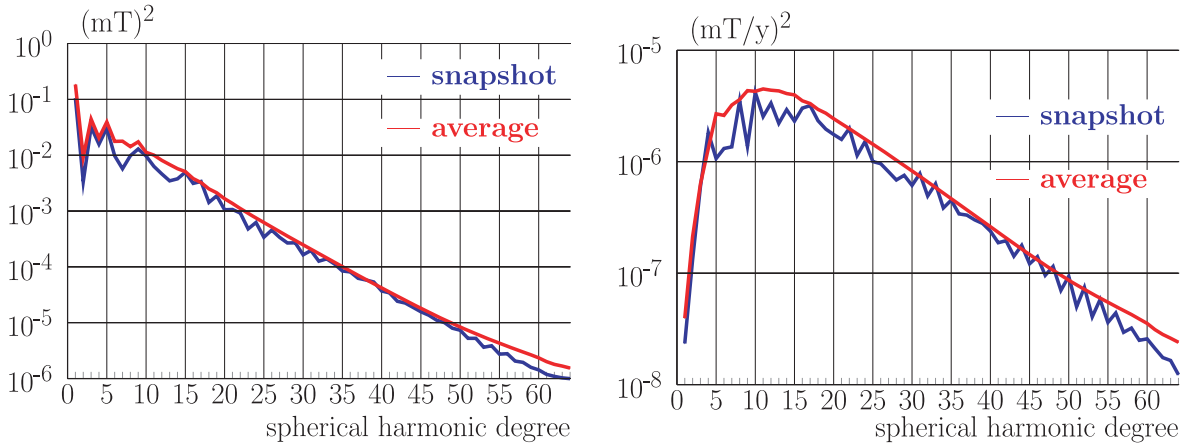

Figure 2. Mauersberger–Lowes spectra at the core–mantle boundary for the field (left-hand panel) and the secular variation (right-hand panel) generated by the dynamo model (logarithmic scales), after application of the scaling procedure described in the text. In blue: instantaneous spectra for a randomly picked sample. In red: time-averaged spectra.

It suffers from being based on a single coefficient (the axial dipole), which is known to behave quite differently from all the others (see, e.g. Hulot *et al.* 2010b). The rms-based scaling avoids this shortcoming, at the expense of not being directly based on observations. Note, however, that Gillet *et al.* (2010a) and Buffett (2010) have recently proposed evidence from observations to support the high-power scenario of Aubert *et al.* (2009) we follow here.

3.2 The state vector for the core flow problem

In this section, we describe the various components of the discrete state vector. These components are expressed in physical units, after application of the various scaling procedures described above. The PARODY-JA code we resort to operates with finite differences in radius and spherical harmonics $\mathcal{Y}_l^m$ in the horizontal directions (Dormy *et al.* 1998; Aubert *et al.* 2008). For the input parameters listed in eq. (14), convergence is achieved by using 90 points in radius, together with a horizontal truncation L set to 64.

We extract from the simulation time-dependent maps of B_r and $\dot{B}_r$ at the core surface, and of $\boldsymbol{u}_h = (u_\phi, u_\theta)$ at the top of the free stream. The horizontal components of the velocity vector are subject to special conditions at the poles ($\theta = 0$ or π). Following common practice, we resort to a modified velocity field $\tilde{\boldsymbol{u}}_h$ which writes

$$\tilde{\boldsymbol{u}}_h(\theta, \phi) = \sin\theta \, \boldsymbol{u}_h(\theta, \phi), \tag{21}$$

and whose components possess the properties of scalar fields on the sphere and are therefore suitable for a standard spherical harmonic transform (e.g. Boyd 2001, section 18.9). In physical space, the use of Gaussian–Legendre quadrature points in the θ direction ensures the well posedness of the reciprocal transform $\boldsymbol{u}_h = (\sin\theta)^{-1}\tilde{\boldsymbol{u}}_h$. The expansion of each field is written as

$$(B \equiv B_r, \dot{B} \equiv \dot{B}_r, \tilde{u}_\phi, \tilde{u}_\theta) = \sum_{l=0}^{L} \sum_{m=-l}^{l} (B_{lm}, \dot{B}_{lm}, \tilde{u}_{\phi,lm}, \tilde{u}_{\theta,lm}) \mathcal{Y}_l^m(\theta, \phi),$$

in which each set of coefficients is complex-valued, the spherical harmonics themselves being fully normalized. We operate in spectral space and define accordingly our state vector $\mathbf{x}$ (a column vector) as

$$\mathbf{x} = \left[\ldots, B_{lm}, \ldots, \dot{B}_{lm}, \ldots, \tilde{u}_{\phi,lm}, \ldots, \tilde{u}_{\theta,lm}, \ldots \right]^T. \tag{22}$$

Given that $L = 64$, the size of the complex-valued state vector is 8580. Fig. 3(left-hand column) shows the representation of the state vector in physical space, for a state vector randomly picked in the time window used to derive the statistics of the numerical dynamo model.

The large value of the magnetic Prandtl number (4, see above) results in narrow magnetic patches concentrated in the mid-latitudes (see Fig. 3a), a situation unlikely to occur at the surface of the core, where one expects that magnetic flux patches should be distributed over areas larger than the surficial imprint of convective columns. The secular variation $\dot{B}_r$ results from the westward drift of these patches at the surface of the core (see Fig. 3b), and is consequently concentrated along the rims of these patches. The flow, shown in Figs 3(c) and (d), is the surficial signature of the convective columns, with energy predominantly present around azimuthal wavenumbers $m = 3$, 4 and 5.

Recently, Christensen *et al.* (2010) have defined a series of quantitative static morphological criteria to help define what would be a good candidate model to represent the current geomagnetic field. They consider the ratio of the power in the axial dipole component to that in the rest of the field, the ratios between equatorially symmetric and antisymmetric and between zonal and non-zonal non-dipole components, and a measure for the degree of spatial concentration of magnetic flux at the core surface. We have estimated the morphological quality of our model according to these criteria, and Table 1 shows the corresponding score. This overall score (>5) shows that the model is marginally bad according to Christensen *et al.* (2010), essentially because of the too large value of the flux concentration factor resulting from the large value of the magnetic Prandtl number.

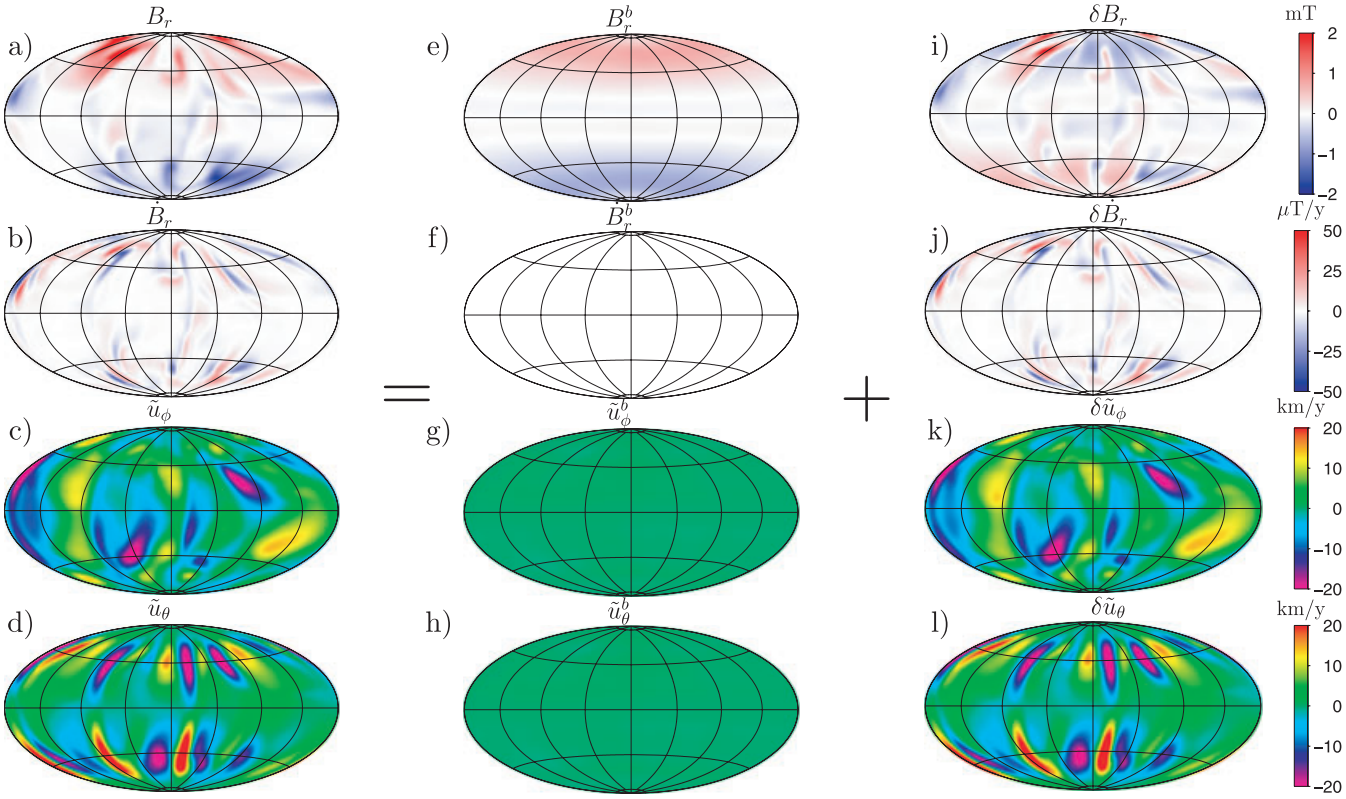

Figure 3. A snapshot of the state vector for the core flow problem (extracted from the 3-D simulation) after the scaling described in the text has been applied. (a) The radial magnetic induction at the top of the core, B_r. (b) Its rate-of-change $\dot{B}_r$. (c) The (modified) eastward component of the flow at the top of the free stream. (d) The (modified) southward component of the flow at the top of the free stream. The state vector is decomposed as the sum of a mean state (centre column) and a departure about that mean state (right-hand column). The mean and the departure are plotted using the same colour scale, which shows that the only significant contribution to the mean is that of B_r, which has an amplitude on the order of 1 mT.

Table 1. The rating of the dynamo model according to Christensen *et al.* (2010). This rating is based on the degree of semblance of the large-scale morphology of the dynamo field with that of the geomagnetic field. The four criteria, whose quantitative definitions are provided by Christensen *et al.* (2010), are given different weights, in proportions detailed in Christensen *et al.* (2010).

Property	Value	Target	σ	χ^2
Relative axial dipole power	1.13	1.40	2.00	0.10
Equatorial symmetry	1.90	1.00	2.00	0.86
Zonality	0.45	0.15	2.50	2.05
Flux concentration	4.40	1.50	1.75	3.07
Total				6.08

3.3 The background state vector $\mathbf{x}^b$ and the background covariance matrix $\mathbf{P}^b$

To determine the background state $\mathbf{x}^b$, we take the $N_e = 18\,000$ samples of the state vector $\mathbf{x}_i$ we extracted from the integration of the numerical model, and define

$$\mathbf{x}^b = \frac{1}{N_e} \sum_{i=1}^{N_e} \mathbf{x}_i . \tag{23}$$

The width of the time window was chosen in order to obtain converged statistics. For a given window width T, and for every spectral coefficient of the state vector a_{lm}, we estimated the convergence by computing running averages of the form

$$\overline{a}_{lm}(T) = \frac{1}{T} \int_0^T a_{lm}(t) \mathrm{d}t, \tag{24}$$

and chose T such that the above quantity was not varying by more than a percent for all a's. The axial dipole coefficient B_{10} turned out to be the less rapidly converging coefficient. We stopped the run upon checking that the relative changes in its running average were smaller than 1 per cent during the last 50 000 yr of the 240 270 yr of model integration.

The sampling rate or, equivalently, the number of samples, must be such that two contiguous samples do not miss any dynamic event. We found that for the statistics to be unaltered, the time between two successive samples, ΔT_S, should be smaller than the *e*-folding time characterizing the simulation (Hulot *et al.* 2010a; Lhuillier *et al.*, in preparation), which happens to be 350 yr for our model. $N_e = 18\,000$ corresponds to a conservative value of $\Delta T_S \sim 13$ yr, and all the results we shall describe were obtained using this value.

We define next the increment $\delta \mathbf{x}_i$ for any given sample i as

$$\delta \mathbf{x}_i \equiv \mathbf{x}_i - \mathbf{x}^{\mathrm{b}}. \tag{25}$$

Fig. 3 shows an illustration of the decomposition of the state in its mean plus a fluctuation. It is noteworthy that the mean is essentially zero for the secular variation and the two components of the flow (Figs 3f–h). As far as the field B_{r} is concerned (Fig. 3e), the numerical model has a constant polarity, and the mean is almost perfectly zonal, with peak values of about ± 1 mT, and a zero mean field inside the tangent cylinder (the imaginary cylinder circumscribing the inner core and parallel to the axis of rotation of the Earth). The smallness of the mean flow at the top of the free stream can be attributed to the weakness of the chemical forcing and to the lateral homogeneity of the boundary conditions for codensity on the outer boundary.

The variability about the background state (i.e. the variability of $\delta \mathbf{x}$) is further illustrated in Fig. 4, where histograms of some spectral coefficients of the various components of $\delta \mathbf{x}$ are represented. The shapes of the histograms suggest that the hypothesis of Gaussianity made in Section 2 is reasonable, save for two coefficients (out of the several thousands), which are shown in Fig. 4. The coefficient corresponding to the axial dipole (which is slightly skewed and biased) and a coefficient for the longitudinal flow, which is bimodal. To go any further, we need to accept these deviations from Gaussianity, and the loss of optimality, since it is no longer possible to associate, in a Bayesian framework, our solution with the maximum of the a posteriori pdf. Still, we should remind ourselves that the solution provided by eqs (12) or (13) remains, from a stochastic inversion perspective, the minimum variance estimation compatible with the statistics supplied by $\mathbf{P}^{\mathrm{b}}$ and $\mathbf{R}$ (see, e.g. Jackson 1979; Wunsch 2006).

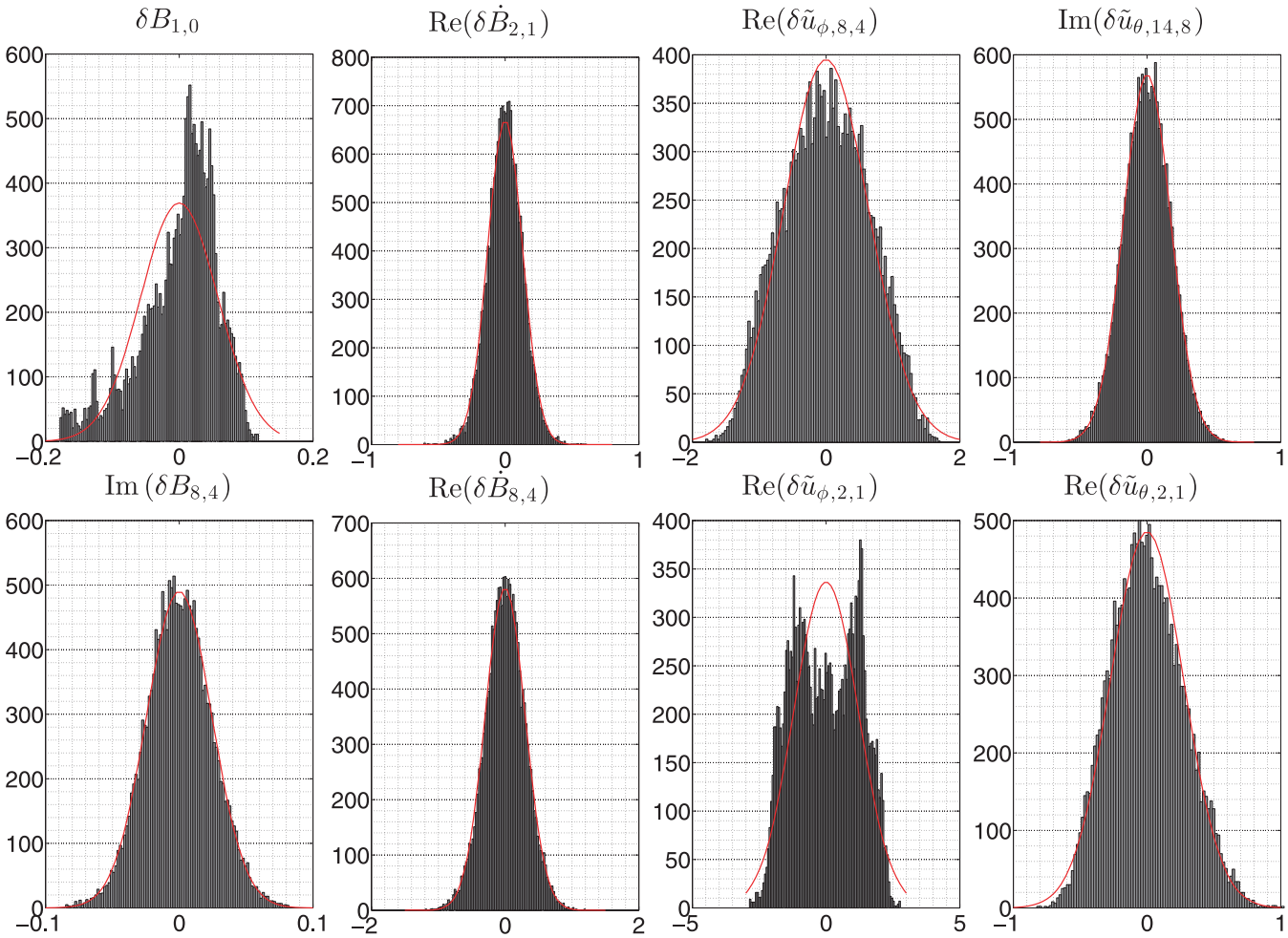

Figure 4. Histograms showing the distribution of some of the 8 580 coefficients of the incremental state vector $\delta \mathbf{x}$. The units on the *x*-axis are mT, μT yr^{-1}, and km yr^{-1} for δB_{lm}, $\delta \dot{B}_{lm}$, and $\delta \tilde{u}_{\phi,lm}$ and $\delta \tilde{u}_{\theta,lm}$, respectively. For each histogram, a fit by a normal law is shown with a red line.

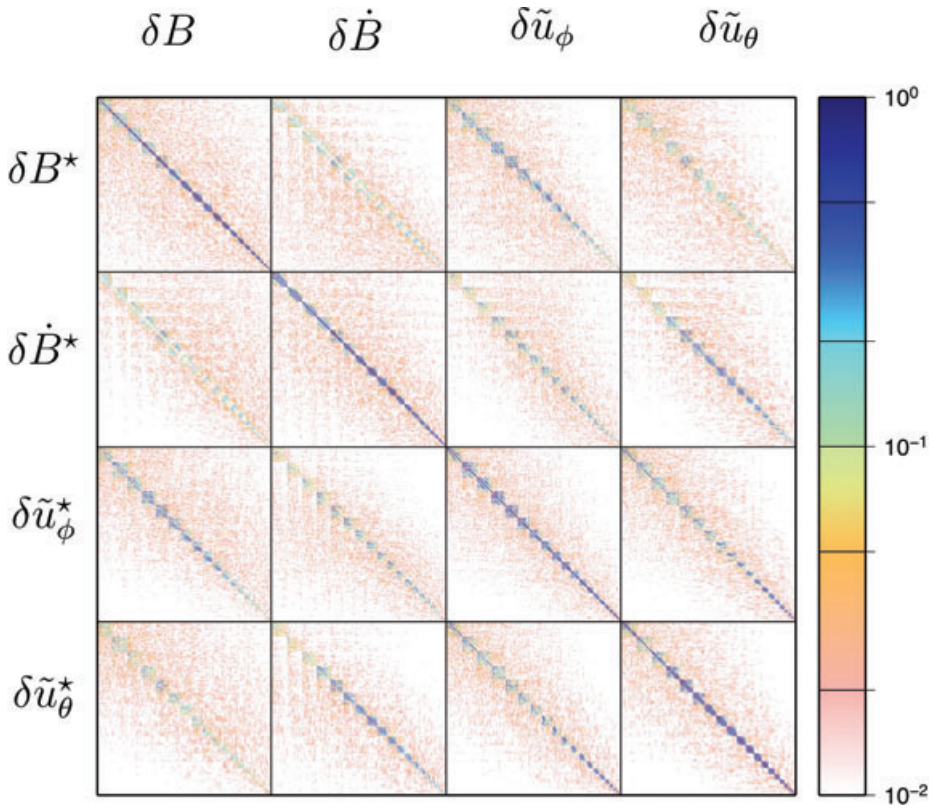

Figure 5. A normalized view of the background covariance matrix $\mathbf{P}^{\mathrm{b}}$, for which every coefficient involved in the calculation has been normalized by its variance. To allow for visual inspection, this representation is truncated, in the sense that the truncation for each field has been set to 20, as opposed to the value of 64 effectively used in this study. $\mathbf{P}^{\mathrm{b}}$ is a 4×4 block matrix which expresses the multivariate relationship between the magnetic field, its rate-of-change, and the flow.

Turning next our attention to the background error covariance matrix which appears in the definition of the objective function (eq. 10), we define it as

$$\mathbf{P}^{\mathrm{b}} = \frac{1}{N_e - 1} \left[\begin{array}{c|c|c|c} \delta B^\star_{lm,i}\delta B_{l'm',i} & \delta B^\star_{lm,i}\delta \dot{B}_{l'm',i} & \delta B^\star_{lm,i}\delta \tilde{u}_{\phi,l'm',i} & \delta B^\star_{lm,i}\delta \tilde{u}_{\theta,l'm',i} \\ \hline \delta \dot{B}^\star_{lm,i}\delta B_{l'm',i} & \delta \dot{B}^\star_{lm,i}\delta \dot{B}_{l'm',i} & \delta \dot{B}^\star_{lm,i}\delta \tilde{u}_{\phi,l'm',i} & \delta \dot{B}^\star_{lm,i}\delta \tilde{u}_{\theta,l'm',i} \\ \hline \delta \tilde{u}^\star_{\phi,lm,i}\delta B_{l'm',i} & \delta \tilde{u}^\star_{\phi,lm,i}\delta \dot{B}_{l'm',i} & \delta \tilde{u}^\star_{\phi,lm,i}\delta \tilde{u}_{\phi,l'm',i} & \delta \tilde{u}^\star_{\phi,lm,i}\delta \tilde{u}_{\theta,l'm',i} \\ \hline \delta \tilde{u}^\star_{\theta,lm,i}\delta B_{l'm',i} & \delta \tilde{u}^\star_{\theta,lm,i}\delta \dot{B}_{l'm',i} & \delta \tilde{u}^\star_{\theta,lm,i}\delta \tilde{u}_{\phi,l'm',i} & \delta \tilde{u}^\star_{\theta,lm,i}\delta \tilde{u}_{\theta,l'm',i} \end{array} \right], \tag{26}$$

adopting Einstein's conventions on repeated indices. Fig. 5 shows this matrix in a normalized and truncated version (for which every coefficient entering the definition above has been divided by its variance, and the truncation set to 20, as opposed to 64); in fact, the matrix effectively used in our calculations (defined by eq. 26), does not lend itself easily to visual inspection, because of its size, of the mixing of units, and of the disparity in the amplitude of the variations of the various coefficients defining $\delta\mathbf{x}$.

The lexicographical ordering we use to define a single integer index k from the values of (l, m) is such that for a given m, k increases with l (k becomes $k + 1$ when l becomes $l + 1$). When l reaches the value m, m becomes $m + 1$, l becomes 0, k becomes $k + 1$, then k becomes $k + 1$ when l becomes $l + 1$, and so on, and so forth. Each of the 16 blocks which define $\mathbf{P}^b$ displays a block diagonal structure, each diagonal sub-block being associated with a given azimuthal wavenumber m. This shows that the correlations between the various components of $\delta\mathbf{x}$ are mostly confined inside each Fourier mode: for instance δB_{lm} will be sensitive to changes in $\delta B_{l'm}(l' \neq l)$, and not sensitive to changes in $\delta B_{lm'}(m' \neq m)$. The strongest correlations between the field (or the secular variation) and the flow are seen in the $m = 3, 4$ or 5 sub-blocks, the dominant modes of convection of this model. The correlations between the field and the secular variation are due to non-linear interactions (eq. 1), which reflects itself in the white diagonal of the corresponding sub-blocks in Fig. 5. Finally, one can notice in passing that the four blocks along the main diagonal are not rigorously diagonal matrices, confirming that a dynamo model, when considered over a time span of a few thousands years, is close to being, but is not exactly, a giant gaussian process (Constable & Parker 1988; Bouligand *et al.* 2005).

The full 8580×8580 $\mathbf{P}^{\mathrm{b}}$ matrix is not diagonal, and it exhibits a poor conditioning. Consequently, in the following, we shall resort to eq. (13) to compute the Kalman gain, since it does not require the direct calculation of $\mathbf{P}^{\mathrm{b}^{-1}}$ (and even more so since the size of the observation vector $N_{\mathbf{y}^{\mathrm{o}}}$ is much smaller than the size of the state vector, $N_{\mathbf{x}}$, recall Section 2).[1]

[1] Correction added after online publication 2011 May 19: in the preceding sentence '$N_{\mathbf{y}^{\mathrm{b}}}$' has been corrected to '$N_{\mathbf{y}^{\mathrm{o}}}$'.

4 EXPERIMENTS WITH SYNTHETIC DATA

We begin by testing the validity of the implementation of our methodology by using synthetic data based on the numerical dynamo model which defines our prior. Since observations in this study consist of geomagnetic field models at the CMB, we define as our synthetic data the spectral coefficients associated with maps of $B_{\rm r}$ and $\dot{B}_{\rm r}$ for each of the $N_e = 18\,000$ samples taken from the numerical dynamo model, to which we add some noise, and which we truncate at spherical harmonic degree 14 (this corresponds roughly to the degree up to which geomagnetic field models based on real magnetic measurements are assumed to be realiably represented; see for instance Gillet *et al.* (2010b)). In practice, we therefore add to every sample i Gaussian noises $\boldsymbol{\epsilon}^o_{B,i}$ and $\boldsymbol{\epsilon}^o_{\dot{B},i}$ of amplitude 0.001 mT and 0.001 mT yr^{-1} for $B_{\rm r}$ and $\dot{B}_{\rm r}$, respectively. Note that $\boldsymbol{\epsilon}^o_B$ and $\boldsymbol{\epsilon}^o_{\dot{B}}$ are added on the physical Gauss–Legendre–Fourier grid. The matrix $\mathbf{R}$ (which involves the spectral coefficients of the observation error) is constructed by computing the spectral transform of this noise for every single snapshot, $\boldsymbol{\epsilon}^o_{B,lm,i}$ and $\boldsymbol{\epsilon}^o_{\dot{B},lm,i}$. We build accordingly

$$\mathbf{R} = \frac{1}{N_e - 1} \begin{bmatrix} \boldsymbol{\epsilon}^{\mathrm{o}\star}_{B,lm,i}\boldsymbol{\epsilon}^{\mathrm{o}}_{B,l'm',i} & \boldsymbol{\epsilon}^{\mathrm{o}\star}_{B,lm,i}\boldsymbol{\epsilon}^{\mathrm{o}}_{\dot{B},l'm',i} \\ \boldsymbol{\epsilon}^{\mathrm{o}\star}_{\dot{B},lm,i}\boldsymbol{\epsilon}^{\mathrm{o}}_{B,l'm',i} & \boldsymbol{\epsilon}^{\mathrm{o}\star}_{\dot{B},lm,i}\boldsymbol{\epsilon}^{\mathrm{o}}_{\dot{B},l'm',i} \end{bmatrix}, \tag{27}$$

adopting again Einstein's convention on repeated indices. The truncation at spherical harmonic degree 14 implies that the size of the observation vector $\mathbf{y}^{\mathrm{o}}$ is 240. Since we operate in spectral space, the observation operator $\mathbf{H}$ is rectangular (240 $\times$ 8580), filled with 240 'one' entries and zeros for the rest. The Kalman gain matrix $\mathbf{K}$ defined by eq. (13) is 8 580 $\times$ 240. For each of the 18 000 noised observations we generated, $\mathbf{K}$ makes it possible to estimate the state vector, and to compare this estimate $\widehat{\mathbf{x}}_i$ with the known true state $\mathbf{x}^t_i \equiv \mathbf{x}_i$. In Fig. 6 (left-hand panel), we plot the innovation vector $\mathbf{y}^{\mathrm{o}} - \mathbf{H}\,\mathbf{x}^{\mathrm{b}}$ for one given sample, on which we will focus our attention in the remainder of this section (each sample leads to similar conclusions). In the same figure (centre panel), we plot the residual vector, defined as $\mathbf{H}[\mathbf{x}^t - (\widehat{\delta\mathbf{x}} + \mathbf{x}^{\mathrm{b}})]$ in which $\widehat{\delta\mathbf{x}}$ is given by $\widehat{\delta\mathbf{x}} = \mathbf{K}(\mathbf{y}^{\mathrm{o}} - \mathbf{H}\mathbf{x}^{\mathrm{b}})$. For reference, the observed part of the noise that was added to the field and its rate-of-change for this specific sample is shown in the right panel. For both the radial component and its secular variation, the action of the Kalman gain yields residuals that are easily identified as coming from the leakage of the random error into the recovered geomagnetic model for degrees 1–14 (compare the centre and right-hand panels in Fig. 6).

After this initial inspection of the observed part of the state vector, let us now turn our attention to the estimation of the whole state vector, $\widehat{\mathbf{x}} = \widehat{\delta\mathbf{x}} + \mathbf{x}^{\mathrm{b}}$. Fig. 7 shows the four components of the true state vector and of its estimate in the left and centre panels, respectively. There is a good visual agreement between the true state and its estimate. The large scales of $B_{\rm r}$ and $\dot{B}_{\rm r}$ (which both define the observations) are correctly recovered as described above; the differences are essentially to be found in the small scales. This is especially true for the secular variation, some small-scale features of which are absent in the estimate. The estimates of $\tilde{u}_\phi$ and $\tilde{u}_\theta$ are also similar to their true counterparts, even though some of the features of the true state do not appear in the estimate. This nevertheless shows that the multivariate analysis upon which $\mathbf{P}^{\mathrm{b}}$ relies makes it possible to produce a satisfactory estimate of the unobserved components of the state vector. We can make a more quantitative assessment, beginning with the energetic spectra of the true and estimated states (see the right-hand panel in Fig. 7). For the magnetic field and its rate-of-change, we compute the Mauersberger–Lowes spectra. For the (modified) flow $\tilde{\boldsymbol{u}}_h$, we compute the energy in each azimuthal Fourier mode m. These various spectra demonstrate a reasonable energetic agreement for the four components of the state vector in the first 10 degrees (or orders). In this range, the information contained in the observations dominates that contained in

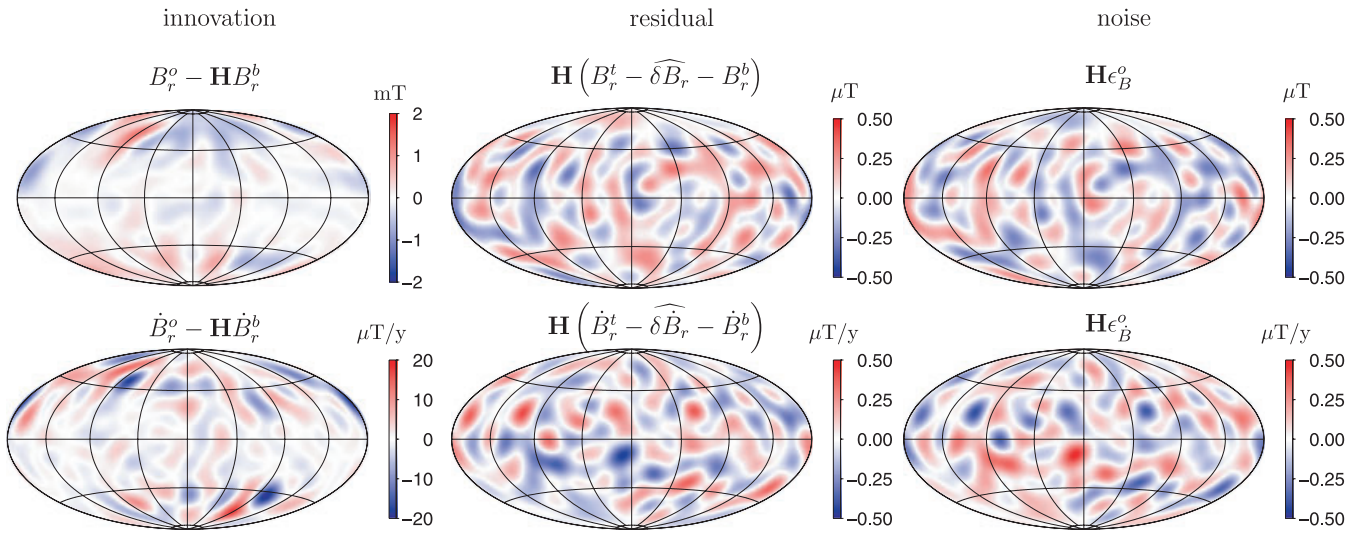

Figure 6. Left-hand panel: the initial difference (the innovation) between the synthetic data and the model prediction (based only on the background state), for one of the N_e synthetic experiments we carried out. Top: innovation for the radial component of the magnetic field $B_{\rm r}$. Bottom: innovation for its time derivative $\dot{B}_{\rm r}$. Centre panel: the difference (the residual), after inversion, between the observed part of the true state and its estimate. Top: residual for $B_{\rm r}$. Bottom: residual for $\dot{B}_{\rm r}$. Right-hand panel: the observed part of the noise that was added to the true state to define the observations for the synthetic experiments. Top: noise added to $B_{\rm r}$. Bottom: noise added to $\dot{B}_{\rm r}$. Note that all fields, including the noise, are shown up to spherical harmonic degree 14.

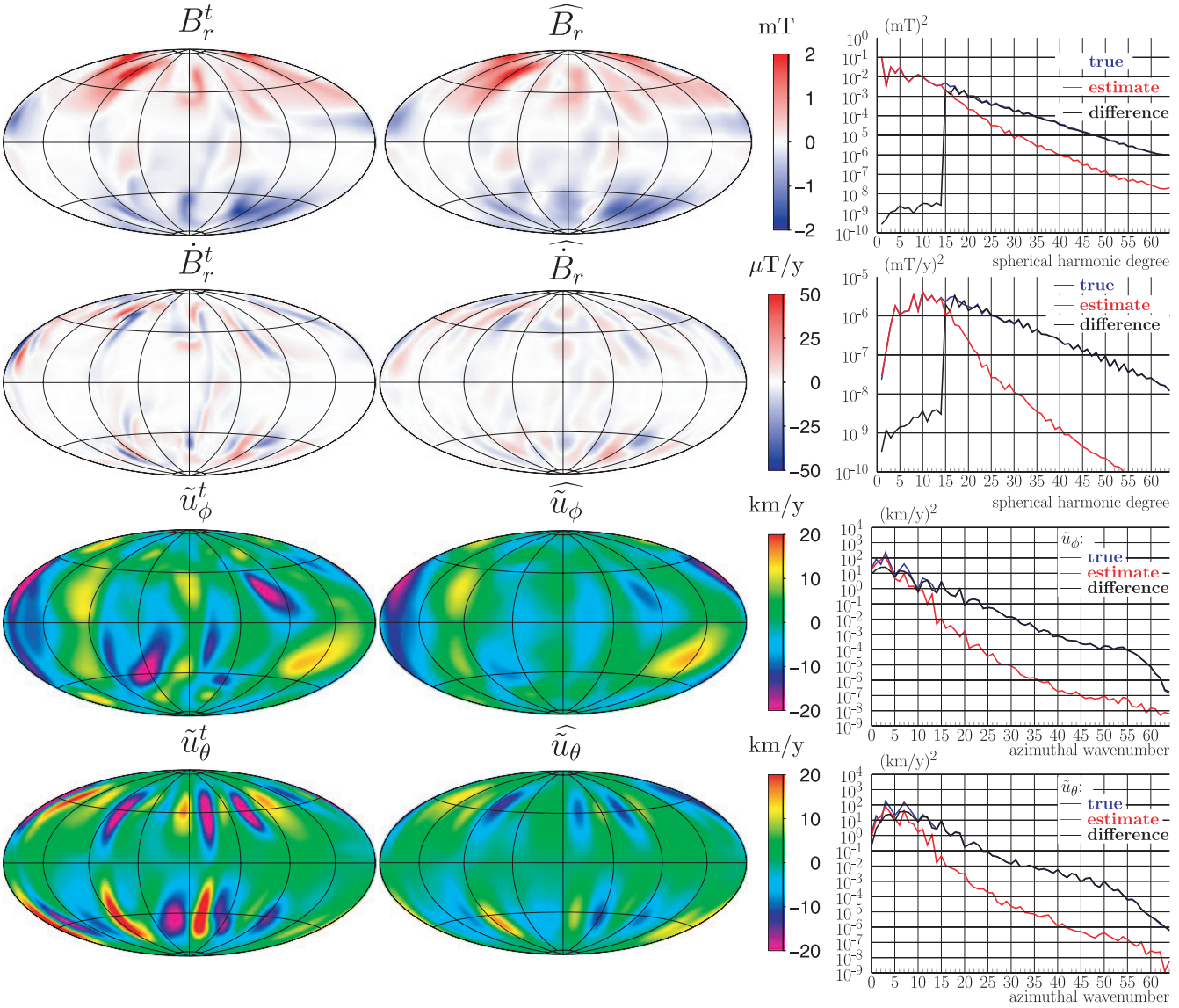

Figure 7. Left-hand panel: the reference state used in one synthetic data experiment (the same as the one used in Fig. 6). Centre panel: its estimate after applying the Kalman gain matrix on the innovation field. Right-hand panel, from top to bottom: Mauersberger–Lowes spectra for the field, the secular variation, and Fourier spectra for the two modified flow components.

the background term, and it prescribes the energetic level of field and flow. Above degree (or order) 10, the background term in the objective function (eq. 10) takes over and acts effectively as a norm: the energetic trend is is the one contained in the prior, but it is damped.

Next, focussing on the full flow recovery, we compute the correlation coefficient

$$C = \frac{\int_S \boldsymbol{u}_h^{\mathrm{t}} \cdot \widehat{\boldsymbol{u}}_h \mathrm{d}S}{\left[\int_S \boldsymbol{u}_h^{\mathrm{t}} \cdot \boldsymbol{u}_h^{\mathrm{t}} \mathrm{d}S \int_S \widehat{\boldsymbol{u}}_h \cdot \widehat{\boldsymbol{u}}_h \mathrm{d}S\right]^{1/2}} \tag{28}$$

and the point recovery factor

$$P = 1 - \frac{\int_S |\boldsymbol{u}_h^{\mathrm{t}} - \widehat{\boldsymbol{u}}_h| \mathrm{d}S}{\int_S |\boldsymbol{u}_h^{\mathrm{t}} + \widehat{\boldsymbol{u}}_h| \mathrm{d}S}, \tag{29}$$

over the surface of the core S, where $\widehat{\boldsymbol{u}}_h$ is the estimated flow, $\boldsymbol{u}_h^{\mathrm{t}}$ is the known true flow, and as suggested by Rau *et al.* (2000) and Amit *et al.* (2007), respectively. For the sample we singled out, we find $C = 0.82$ and $P = 0.67$; both those values are sufficiently close to 1 to indicate a good recovery. Considering our complete collection of N_e synthetic experiments, we find C in the range [0.62–0.94], with a mean value of 0.86. Similarly, the point recovery factor, which is supposedly more sensitive to errors in the estimated amplitude than the correlation coefficient, lies in the range [0.40–0.83], with a mean value of 0.71.

In summary, these numerical experiments with synthetic data demonstrate the feasibility of exploiting the multivariate statistical information contained in the background covariance matrix in order to map the observed parts of the state vector onto its unobserved components. In the case of synthetic data possessing the same properties as the background dynamo simulation, the recovery is satisfactory.

The good recovery of the flow can be explained by the fact that it is large-scale, that it yields a secular variation whose energy lies essentially between spherical harmonic degrees 4 and 20 (recall Fig. 2), and that we observe B_r and $\dot{B}_r$ up to degree 14.

5 CORE FLOW ESTIMATE BASED ON A GEOMAGNETIC FIELD MODEL

We now wish to understand the compatibility between our background numerical dynamo model and a geomagnetic field model, by estimating a core surface flow following the multivariate analysis described earlier. We thus consider a main field model which provides us with a set of Gauss coefficients g_l^m and h_l^m describing the magnetic potential at the surface of the Earth ($r = a = 6371.2$ km), as well as with their time derivatives, $\dot{g}_l^m$ and $\dot{h}_l^m$, for epoch 2010.

It is of practical importance to note that the relationship between the B_{lm} (defined at the CMB) of the state vector introduced in Section 3.2 and the Gauss coefficients (g_l^m, h_l^m) (defined at the surface of the Earth for Schmidt quasi-normalized spherical harmonics) is given by

$$B_{lm} = \frac{l+1}{\sqrt{2l+1}} \left(\frac{a}{c}\right)^{l+2} \left(g_l^m - \mathrm{i} h_l^m\right). \tag{30}$$

The same relationship applies for the coefficients describing the secular variation. For a given truncation L, we can accordingly introduce a rectangular, complex-valued, matrix $\mathbf{G}_a^c(L)$ such that

$$[\ldots B_{lm} \ldots]^T = \mathbf{G}_a^c(L)[\ldots g_{lm}\ h_{lm} \ldots]^T. \tag{31}$$

5.1 Construction of the observation error covariance matrix R

To assemble the Kalman gain matrix, we need to specify the error covariance matrix **R** related to the uncertainty affecting the sets of Gauss coefficients. This requires to look closely at the way the geomagnetic field model is built. We consider a parent model of a candidate to the 11th generation of the International Geomagnetic Reference Field Model (Finlay *et al.* 2010). Details of this model regarding in particular the vector and scalar CHAMP (Reigber *et al.* 2002) satellite data selection, its coverage, and the various hypotheses entering the resolution of the inverse problem that determines the Gauss coefficients are described by Thébault *et al.* (2010). However, it is worth stressing that this model describes the main field up to spherical harmonic 15 and the secular variation up to degree 10 for the year 2010.0, and that it is not regularized. Consequently, the objective function used for its least-squares construction is restricted to the misfit to the data and the model covariance matrix can be written as

$$\mathbf{R}_a = \sigma^2 (A^T A)^{-1}, \tag{32}$$

where A is the design matrix relating the set of Gauss coefficients and the appropriately pre-processed CHAMP data. The quantity σ is the estimated standard deviation between the measurements and the model, equal to 5.1 nT. With the help of the matrix $\mathbf{G}_a^c(L)$ introduced in eq. (31), we find that **R** is given by

$$\mathbf{R} = \mathbf{G}\mathbf{R}_a\mathbf{G}^\dagger, \tag{33}$$

in which

$$\mathbf{G} = \begin{bmatrix} \mathbf{G}_a^c(L=15) & 0 \\ 0 & \mathbf{G}_a^c(L=10) \end{bmatrix}. \tag{34}$$

The knowledge of $\mathbf{P}^b$ (defined by eq. 26, and constructed using our 18 000 samples), **R** and **H** makes it possible to construct the Kalman gain matrix **K** and to estimate next the state vector $\widehat{\mathbf{x}}$ compatible with the observations and the numerical model of the geodynamo. We compute accordingly

$$\widehat{\mathbf{x}} = \widehat{\delta\mathbf{x}} + \mathbf{x}^b = \mathbf{K}(\mathbf{y}^o - \mathbf{H}\mathbf{x}^b) + \mathbf{x}^b, \tag{35}$$

where $\mathbf{y}^o$ is the (observation) vector of Gauss coefficients mapped at the CMB and properly normalized, and $\mathbf{x}^b$ is the previously defined background state.

We will analyse sequentially the magnetic and flow components of the estimated state vector $\widehat{\mathbf{x}}$.

5.2 Estimate of the magnetic part of the state vector

We first focus on the observed part of the magnetic component of the state vector. Fig. 8(a) shows the estimate of the field, its rate-of-change is presented in Fig. 8(b), and the corresponding residuals, defined as the difference between the observation and the estimate, are shown in Figs 8(c) and (d), respectively. To focus on the observed part of the state vector, both the field and the field residuals are truncated at $l = 15$, while both the secular variation and the secular variation residuals are truncated at $l = 10$. The field residuals do not exceed 5 per cent for the field itself, but secular variations residuals may locally reach 40 per cent of the secular variation. Regarding B_r, they appear to be mostly involving degree 15, where the confidence in the field model is the smallest (an indication being given by the tendency of the field spectrum to

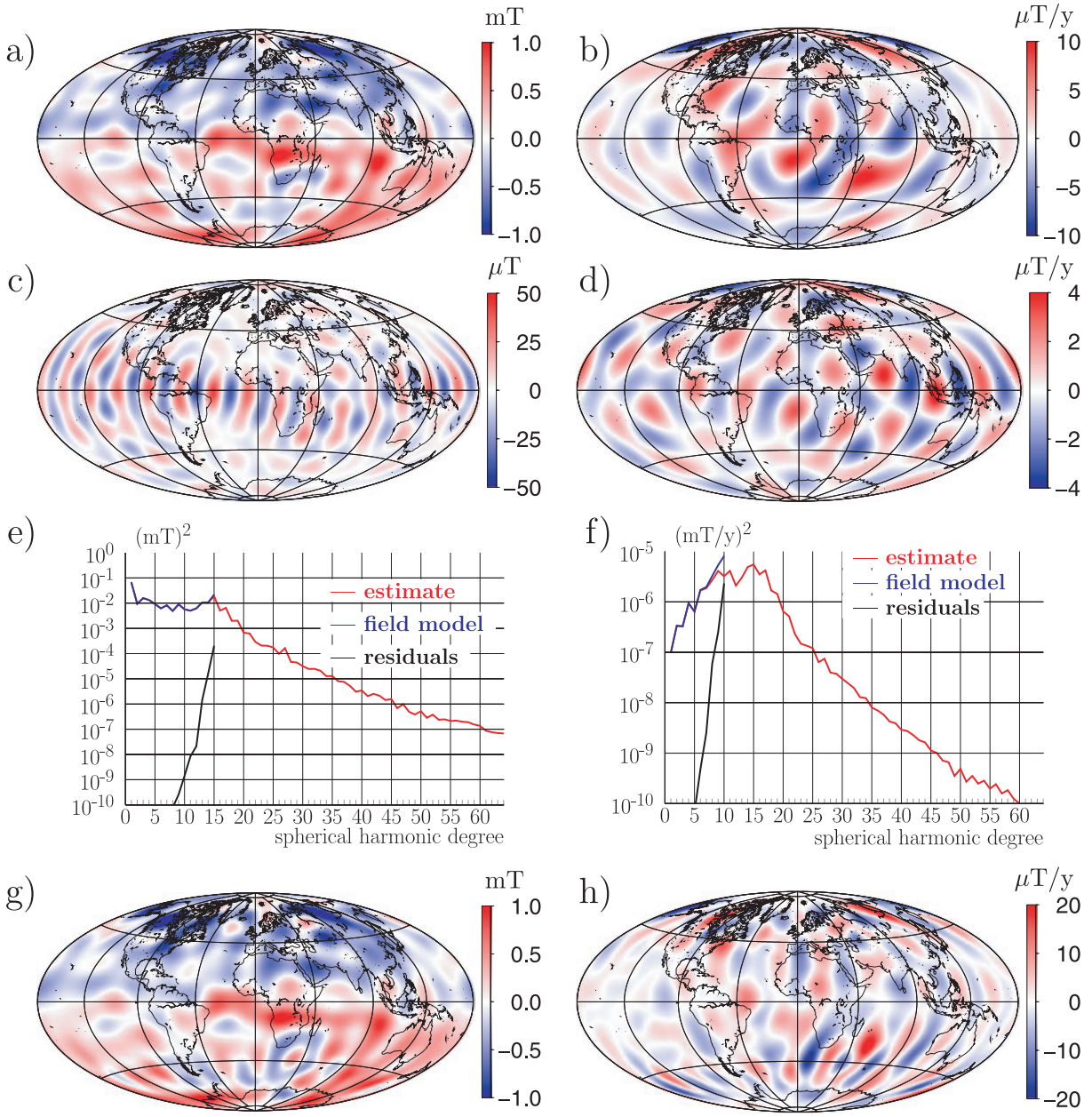

Figure 8. The estimate of the magnetic part of the state vector for epoch 2010. All figures are made at the core–mantle boundary. (a) The radial component of the magnetic induction (truncated at $l = 15$). Peak-to-peak values: [−1.25, 1.06] mT. (b) Its rate-of-change (truncated at $l = 10$). Peak-to-peak values: [−13, 10] μT yr^{-1}. (c) The difference between the map of B_r defined by the reference geomagnetic field model, and the one shown in (a). Peak-to-peak values: [−4.2, 4.4] μT. (d) The difference between the map of $\dot{B}_r$ of the reference geomagnetic field model, and the map shown in (b). Peak-to-peak values: [−3.5, 4.3] μT yr^{-1}. (e) Mauersberger–Lowes spectrum for the field. (f) Mauerserger-Lowes spectrum for the secular variation. For both spectra, the red spectrum corresponds to the observations defined by the reference model, with truncations equal to $l = 15$ and 10 for the field and the secular variation, respectively. The black spectra are those of the full field and secular variation estimates for the state vector (up to $l = 64$). (g) The full estimate of B_r (up to $l = 64$) ; peak-to-peak values: [−1.56, 1.06] mT. (h) The full estimate of $\dot{B}_r$; peak-to-peak values: [−24.4, 22.8] μT yr^{-1}.

go steeply up for $l > 12$, see also the black line in Fig. 8e). That could be the consequence of crustal contamination for those degrees, since the model is constructed at the surface of the Earth. A look at the spectrum for the full estimate (Fig. 8e, red line) reveals that the field spectrum tends to realign itself in just a few degrees with the typical trends seen in Fig. 7. In addition, the concentration of the residuals in the equatorial region is indicative of the absence of an equatorial component in the background field B_r^b (see Fig. 3e). Regarding the rate-of-change of the field, the residuals for $\dot{B}_r$ are mostly to be found around the truncation level ($l = 9 - 10$). Fig. 8(f) shows that the observed and estimated spectra diverge around degree 8. The spectrum for the full estimate of $\dot{B}_r$ (Fig. 8f, red line) is remarkably similar (even for the low degrees) to the one displayed in Fig. 7 in a synthetic context. This agreement is in our view supportive of the scaling procedure described in Section 3.1. Let us now inspect the full (up to $l = 64$) estimate for B_r and $\dot{B}_r$, presented in Figs 8(g) and (h), respectively. Comparing Fig. 8(g) with Fig. 8(a), we find no notable difference regarding the field B_r itself. In agreement with the spectrum shown in Fig. 8(f), $\widehat{\dot{B}}_r$ (Fig. 8h) is on

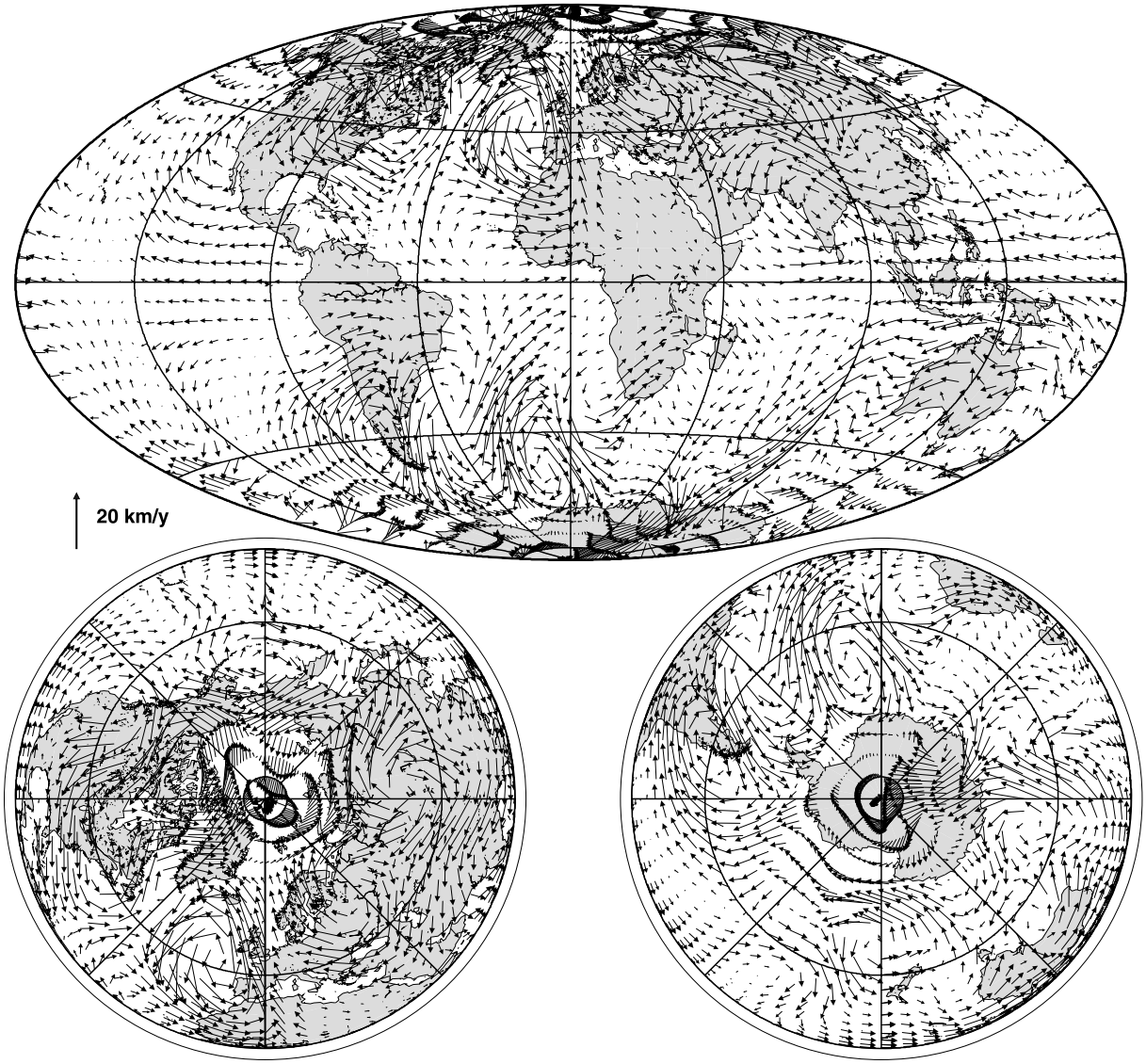

Figure 9. Top panel: the estimated core surface flow $\widehat{\boldsymbol{u}}_h$ at epoch 2010, Hammer projection (maximum amplitude: 22.0 km yr^{-1}). Bottom left-hand panel: The same flow, looking from the North pole. Bottom right-hand panel: looking from the South pole.

the other hand quite energetic in the intermediate scales ($10 \lesssim l \lesssim 20$), and has a maximum amplitude more than twice larger than the one corresponding to the observed part of $\dot{B}_r$, for which $l \leq 10$. The use of the prior information contained in $\mathbf{P}^b$ extends the secular variation spectrum to those scales which are not directly sampled by the observations. The geodynamo model we use is such that the extension of the spectrum consists effectively in adding an important amount of secular variation in the mid-latitudes (where the prior $\dot{B}_r$ is concentrated and rather small scale in latitude, recall Section 3.2 and Fig. 3b). The extra information added by the prior outweighs the information provided by the geomagnetic model. The extension of the spectrum results in a predominantly $m = 5$–6 band of secular variation concentrated in the mid-latitudes (Fig. 8h).

5.3 Core flow estimate

Let us now analyse the flow estimate, which is shown in Fig. 9. Note that plotted here is the 'real' velocity field $\boldsymbol{u}_h$, as opposed to the modified $\tilde{\boldsymbol{u}}_h$ introduced in eq. (21) for numerical expediency. Looking first at the overall flow structure, we note that the most intense flow patterns are located in the mid- to high-latitudes, an observation which is consistent with the typical convective pattern of the numerical model which define our prior information (consider Figs 3c and d). We essentially observe in these latitudes a collection of cyclonic and anticyclonic vortices of varying strength. The stronger vortices are seen in the Atlantic hemisphere (the [90° E, 90° W] longitudinal band), where the observed secular variation is the most intense. In this area, there are two strong circulation foci in the Northern Hemisphere, one underneath North America and one underneath Western Europe. Unlike found by Holme & Olsen (2006) using satellite data (see their Fig. 10a), we find underneath America a cyclonic vortex for epoch 2010. A recent study reporting cyclonic motion underneath North America

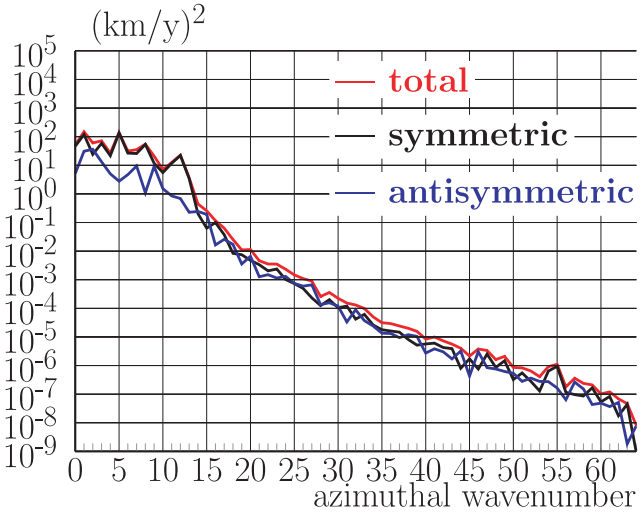

Figure 10. Fourier spectra of the total estimated flow $\widehat{\boldsymbol{u}}_h$ (in red), and of its equatorially symmetric and antisymmetric components in black and blue, respectively.

is the quasi-geostrophic inversion by Pais & Jault (2008), who find as well another cylonic vortex off the West coast of Europe (see their streamfunction map for 2004, in their fig. 11). The equatorial symmetry assumed by Pais & Jault (2008) is such that they find necessarily the same patterns (located outside the tangent cylinder) with opposite rotational sense in the Southern Hemisphere. Our estimate also produces mirror images of these two cyclones in the Southern Hemisphere, but this is not a perfect mirror image. Although the pattern of convection is mostly columnar in our reference dynamo model, it is not perfectly so (recall for instance Fig. 3), to the point here that an anticyclone appears squeezed between the two mirror images of the cyclones. The estimated flow does not exhibit so clearly the signature of convective columns in the Pacific hemisphere, where the observed secular variation is weak. There is an overall westward current located around the Equator, which seems to evolve into a strong southward flow at around 90° W.

To further quantify the level of equatorial symmetry of $\widehat{\boldsymbol{u}}_h$, we now consider its symmetric and antisymmetric components. We show the corresponding azimuthal Fourier spectra in Fig. 10, which represents $\widehat{\boldsymbol{u}}_m^2$ as a function of azimuthal wavenumber m, where $\widehat{\boldsymbol{u}}_m^2$ is defined by the equality

$$\int_S \widehat{\boldsymbol{u}}_h^2 \mathrm{d}S = \sum_{m=0}^{64} \widehat{\boldsymbol{u}}_m^2. \tag{36}$$

From an energetic standpoint, 82 per cent of the flow is equatorially symmetric, a consequence of the convective flow structure in the numerical dynamo model. The Fourier spectrum in Fig. (10) also reveals a substantial amount of kinetic energy in the $m = 1$ mode, which does not appear in the prior (considering the two Fourier spectra in blue in Fig. 7). We interpret this result as the consequence of the strong contrast in the intensity of the secular variation in the Atlantic and Pacific hemisphere.

What our estimate does not show with respect to classical core flow estimates is a large-scale, substantial stream in the ±30° latitudinal band in the Atlantic hemisphere. This type of circulation is nowhere to be found in our model of the geodynamo. This absence, and the fact that the prior is characterized by a rms surface flow on the order of 12 km yr^{-1}, explains why the rms amplitude of $\widehat{\boldsymbol{u}}_h$ is equal to 7.2 km yr^{-1}, a figure smaller by a factor of 2 than typical estimates (Holme 2007). In short, once we have applied the scaling procedure described above, and even though we are quite confident in the scaling procedure itself by inspecting the Mauersberger–Lowes spectra we obtain with or without incorporating geomagnetic observations (Figs 7 and 8e and f), there is not enough energy in the short-time scales of the model for it to yield a core surface flow estimate of amplitude similar to the one obtained with classical approaches.

The specific dynamo model we have chosen is not the best candidate for the exercise we performed, essentially because of the simplicity of its secular variation mechanism (westward transport of very narrow magnetic flux patches concentrated in the mid-latitudes, with almost no secular variation occurring in the equatorial belt). That model was mostly used here to illustrate the generic method we designed. Further work will have to be undertaken with dynamo models possessing a larger degree of semblance with the geodynamo: a larger degree of static semblance such as the one defined by Christensen *et al.* (2010), and a larger degree of dynamic semblance which could be assessed along the lines defined in that study, by inspection of the magnetic residuals and comparison of the estimated core surface flow with classical core surface flow calculations.

6 SUMMARY AND DISCUSSION

We have presented in this paper a framework for using any numerical model of the geodynamo as the prior information for the estimation of core surface flows based on geomagnetic field models. The whole process can be summarized as follows:

(i) Integrate the dynamo model over a long enough time interval to ensure that its running means are converged.

(ii) Upscale the dimensionless outputs of the dynamo model to the Earth, using the scaling laws which you think are relevant for the core flow problem.

(iii) Construct the mean state vector and the background error covariance matrix as defined by $\mathbf{x}^b$ and $\mathbf{P}^b$ in eqs (23) and (26), respectively.

(iv) Use these statistics and the error statistics on the geomagnetic field model, described by the matrix **R** (a good understanding of which is preferable), in order to construct the Kalman gain matrix **K** defined by eq. (13).

(v) Apply the Kalman gain matrix **K** in order to get the estimate of the state of the core compliant with the statistics contained in $\mathbf{P}^b$ and **R**. In practice, the product is an instantaneous estimate for the field B_r and its rate-of-change $\dot{B}_r$ over the entire scale spectrum covered by the dynamo model, along with an instantaneous estimate of the core surface flow, due to the multivariate character of $\mathbf{P}^b$.

Operating in spectral space allows us to have a problem of medium size (requiring 4 gigabytes of memory), which can be handled on a standard workstation, without having to impose any truncation on the state vector other than the truncation used to integrate the dynamo model in the first place (the integration of which admittedly requires more than a single workstation).

We have validated our implementation in the context of synthetic data, and shown in particular the capability of the multivariate statistics embedded in $\mathbf{P}^b$ to help estimate the unobserved components of the state vector (the small scales of the magnetic field, and the flow). The term related to the prior in the misfit function was found to act like a regularization, not unlike previous regularizations (spatial or temporal) introduced in the calculation of core surface flows (see, e.g. Holme 2007, and references therein). With respect to these studies, though, we would like to stress the point that we do not have any flexibility regarding the level of regularity imposed by the prior term in the misfit function, since it is imposed when the scaling has been performed [step (ii) in the list above], and is not directly tuneable.

We have then used a parent model to a recent geomagnetic field model proposed by Thébault *et al.* (2010) for the 11th generation of the IGRF to estimate a core surface flow for epoch 2010. Our motivations for doing so were to use a recent model based on satellite data, while having a good control on the **R** matrix entering our problem. Ideally, one might have wanted to resort to a field model constructed directly at the CMB, but we were mostly interested in that study in assessing the capability of a given dynamo model to yield core surface flow estimates similar to those produced independently using standard approaches. Our model, which we used essentially for illustrative purposes, is not so well suited for this exercise. One would like in particular to see more activity occurring in the equatorial belt.

Further realism will be achieved by pushing numerical dynamo parameters closer to their Earth-like values, in the region of parameter spaces recently delineated by Christensen *et al.* (2010). With the steady increase in computational power, the exploration of this region will become less and less costly in the years to come. One might then expect these models to support secular variation mechanisms closer to what is thought to happen at the surface of the core (see, e.g. Sakuraba & Roberts 2009). Still, the fast torsional oscillations recently put forward by Gillet *et al.* (2010a) seem to be out of reach for these models in the near future, even though some recent high-resolution simulations definitely show hints of wave-like motions (Sakuraba 2010; Wicht & Christensen 2010).

In addition, it would be sensible to define a mean dynamo state $\mathbf{x}^b$ reflecting the thermal control exerted by the mantle on the core (Aubert *et al.* 2007). The related thermal boundary conditions are likely to vary on geological time scales. In that sense, the integration time required to obtain converged statistics should not exceed a value of order 10 Myr. Inhomogeneous thermal boundary conditions would lead to a different background state $\mathbf{x}^b$ (whose flow components might not be almost zero, as was the case here), and logically to a different variability about that background state. The issue of the possible impact of the mantle on the centennial to millennial secular variation of Earth's magnetic field could therefore be addressed within the framework we presented here.

There is an interest in using this framework in order to assess, in light of the observations, the dynamic quality of a given dynamo. Solving the discrete state estimation problem laid out in this study allows one to produce an estimate of the core surface flow at a given epoch, and to compare it with other estimates derived independently. In addition, direct inspection of the field and secular variation residuals can reveal possible shortcomings of the numerical dynamo model. We should comment on the possibility of producing time-dependent estimates, which should carry more dynamic information than snapshot estimates. In this prospect, one might be tempted to resort to geomagnetic observations, as opposed to time-dependent geomagnetic field models, should they cover the archeomagnetic, historical or satellite periods (see, e.g. Hongre *et al.* 1998; Jackson *et al.* 2000; Korte & Constable 2005; Olsen *et al.* 2009). The benefit is to have a better control on the error statistics contained in **R** (which becomes uneasy in case the field model used is regularized in space and/or in time); the price to pay is to resort to the fully dynamic framework of data assimilation, which has recently come to the fore in the context of geomagnetic data analysis (see, e.g. Fournier *et al.* 2010). Recent efforts in trying to assimilate geomagnetic data in dynamic models of the secular variation have essentially followed two trends: one is based on the use of 3-D dynamo models similar to the one presented here (Liu *et al.* 2007; Kuang *et al.* 2008; Kuang *et al.* 2009), while the other is based on the dynamic assumption that the motions responsible for the fast (annual to decadal) variations of the geomagnetic field are quasi-geostrophic (Jault 2008; Canet *et al.* 2009). The latter approach allows one to operate with parameters closer to their Earth-like values than the former, but omit to consider buoyancy in the dynamic balance responsible for the fast motions. The frequency below which the quasi-geostrophic assumption breaks (because of the dynamic input of buoyancy) is unknown, if it breaks at all. As far as the 3-D approach is concerned, it seems logical, in a complementary effort, to start working on the possibility of assimilating historical and archeomagnetic data (Jackson *et al.* 2000; Genevey *et al.* 2008; Donadini *et al.* 2009) to try to better understand and characterize the physics at work behind the long-term (centennial to millennial) geomagnetic secular variation, using an extension of the multivariate framework outlined in this study.

ACKNOWLEDGMENTS

We thank two anonymous reviewers for their input which greatly helped improve the manuscript. This work was supported by INSU through the SEDIT and LEFE ASSIMILATION programs and also in part by the French Centre National d'Études Spatiales (CNES). AF would like to thank Chris Finlay for interesting discussions, Geneviève Moguilny for her help with the LaTeX language, and Florian Lhuillier for his assistance in producing Fig. 4. The plots were created using the generic mapping tools (Wessel & Smith 1991) and the pstricks package (http://en.wikipedia.org/wiki/PSTricks). That is IPGP contribution number 3150.

REFERENCES

Amit, H. & Olson, P., 2004. Helical core flow from geomagnetic secular variation, *Phys. Earth planet. Inter.,* **147**(1), 1–25.

Amit, H., Olson, P. & Christensen, U., 2007. Tests of core flow imaging methods with numerical dynamos, *Geophys. J. Int.,* **168**(1), 27–39.

Arfken, G.B. & Weber, H.J., 1995. *Mathematical Methods for Physicists,* 4th edn, Academic Press, San Diego, CA.

Aubert, J., Amit, H. & Hulot, G., 2007. Detecting thermal boundary control in surface flows from numerical dynamos, *Phys. Earth planet. Int.,* **160**(2), 143–156.

Aubert, J., Aurnou, J. & Wicht, J., 2008. The magnetic structure of convection-driven numerical dynamos, *Geophys. J. Int.,* **172**(3), 945–956.

Aubert, J., Labrosse, S. & Poitou, C., 2009. Modelling the palaeo-evolution of the geodynamo, *Geophys. J. Int.,* **179,** 1414–1428.

Backus, G.E., 1968. Kinematics of geomagnetic secular variation in a perfectly conducting core, *Philo. Trans. R. Soc. Lond. Ser. A, Math. Phys. Sci.,* **263**(1141), 239–266.

Barenblatt, G.I., 1996. *Scaling, Self-Similarity, and Intermediate Asymptotics,* Cambridge University Press, Cambridge.

Bloxham, J. & Jackson, A., 1991. Fluid flow near the surface of Earth's outer core, *Rev. Geophys.,* **29**(1), 97–120.

Bouligand, C., Hulot, G., Khokhlov, A. & Glatzmaier, G.A., 2005. Statistical palaeomagnetic field modelling and dynamo numerical simulation, *Geophys. J. Int.,* **161**(3), 603–626.

Boyd, J.P., 2001. *Chebyshev and Fourier Spectral Methods,* 2nd edn, Dover, Maneola, NY.

Braginsky, S.I. & Roberts, P.H., 1995. Equations governing convection in Earth's core and the geodynamo, *Geophys. astrophys. Fluid Dyn.,* **79**(1), 1–97.

Buffett, B.A., 2010. Tidal dissipation and the strength of the Earth's internal magnetic field, *Nature,* **468**(7326), 952–954.

Canet, E., Fournier, A. & Jault, D., 2009. Forward and adjoint quasi-geostrophic models of the geomagnetic secular variation, *J. geophys. Res.,* **114,** B11101, doi:10.1029/2008JB006189.

Christensen, U.R., 2010. Dynamo scaling laws and applications to the planets, *Space Sci. Rev.,* **152**(1–4), 565–590.

Christensen, U.R. & Aubert, J., 2006. Scaling properties of convection-driven dynamos in rotating spherical shells and application to planetary magnetic fields, *Geophys. J. Int.,* **140,** 97–114.

Christensen, U.R. & Tilgner, A., 2004. Power requirement of the geodynamo from ohmic losses in numerical and laboratory dynamos, *Nature,* **429**(6988), 169–171.

Christensen, U.R., Aubert, J. & Hulot, G., 2010. Conditions for Earth-like geodynamo models, *Earth planet. Sci. Lett.,* **296**(3–4), 487–496.

Constable, C.G. & Parker, R.L., 1988. Statistics of the geomagnetic secular variation for the past 5 Myr, *J. geophys. Res.,* **93,** 11 569–11 581.

Donadini, F., Korte, M. & Constable, C., 2009. Geomagnetic field for 0–3 ka: 1. New data sets for global modeling, *Geochem. Geophys. Geosyst.,* **10,** Q06007, doi:10.1029/2008GC002295.

Dormy, E., Cardin, P. & Jault, D., 1998. MHD flow in a slightly differentially rotating spherical shell, with conducting inner core, in a dipolar magnetic field, *Earth planet. Sci. Lett.,* **160**(1–2), 15–30.

Eymin, C. & Hulot, G., 2005. On core surface flows inferred from satellite magnetic data, *Phys. Earth planet. Int.,* **152,** 200–220.

Finlay, C.C. *et al.*, 2010. International geomagnetic reference field: the eleventh generation, *Geophys. J. Int.,* **183**(3), 1216–1230.

Fournier, A. *et al.*, 2010. An introduction to data assimilation and predictability in geomagnetism, *Space Sci. Rev.,* **155**(1–4), 247–291, doi:10.1007/s11214-010-9669-4.

Genevey, A., Gallet, Y., Constable, C., Korte, M. & Hulot, G., 2008. ArcheoInt: an upgraded compilation of geomagnetic field intensity data for the past ten millennia and its application to the recovery of the past dipole moment, *Geochem. Geophys. Geosyst.,* **9**(4), Q04038, doi:10.1029/2007GC001881.

Gillet, N., Pais, A. & Jault, D., 2009. Ensemble inversion of time-dependent core flow models, *Geochem. Geophys. Geosyst.,* **10,** Q06004, doi:10.1029/2008GC002290.

Gillet, N., Jault, D., Canet, E. & Fournier, A., 2010a. Fast torsional waves and strong magnetic field within the Earth's core, *Nature,* **465,** 74–77.

Gillet, N., Lesur, V. & Olsen, N., 2010b. Geomagnetic core field secular variation models, *Space Sci. Rev.,* **155**(1–4), 129–145, doi:10.1007/s11214-009-9586-6.

Gubbins, D., 1982. Finding Core Motions from Magnetic Observations, *Philo. Trans. R. Soc. Lond. A,* **306,** 247–254.

Gubbins, D., 1983. Geomagnetic field analysis – I. Stochastic Inversion, *Geophys. J. R. astr. Soc.,* **73,** 641–652.

Holme, R., 2007. Large-scale flow in the core, in *Core Dynamics,* Vol. 8: Treatise on Geophysics, pp. 107–130, eds Olson, P. & Schubert, G., Elsevier, Amsterdam.

Holme, R. & Olsen, N., 2006. Core surface flow modelling from high-resolution secular variation, *Geophys. J. Int.,* **166**(2), 518–528.

Hongre, L., Hulot, G. & Khokhlov, A., 1998. An analysis of the geomagnetic field over the past 2000 years, *Phys. Earth planet. Int.,* **106**(3), 313–336.

Hulot, G. & Le Mouël, J.-L., 1994. A statistical approach to the Earth's main magnetic field, *Phys. Earth planet. Int.,* **82**(3), 167–184.

Hulot, G., Eymin, C., Langlais, B., Mandea, M. & Olsen, N., 2002. Small-scale structure of the geodynamo inferred from Oersted and Magsat satellite data, *Nature,* **416**(6881), 620–623.

Hulot, G., Lhuillier, F. & Aubert, J., 2010a. Earth's dynamo limit of predictability, *Geophys. Res. Lett.,* **37,** L06305, doi:10.1029/2009GL041869.

Hulot, G., Finlay, C.C., Constable, C.G., Olsen, N. & Mandea, M., 2010b. The magnetic field of planet Earth, *Space Sci. Rev.,* **152**(1–4), 159–222.

Jackson, A., 1997. Time-dependency of tangentially geostrophic core surface motions, *Phys. Earth planet. Int.,* **103,** 293–311.

Jackson, A., Bloxham, J. & Gubbins, D., 1993. Time-dependent flow at the core surface and conservation of angular momentum in the coupled core–mantle system, in *Dynamics of Earth's Deep Interior and Earth Rotation,* pp. 97–107, American Geophysical Union, Washington, DC.

Jackson, A., Jonkers, A. & Walker, M., 2000. Four centuries of geomagnetic secular variation from historical records, *Philo. Trans. R. Soc. Ser. A: Math., Phys. Eng. Sci.,* **358**(1768), 957–990.

Jackson, D.D., 1979. The use of a priori data to resolve non-uniqueness in linear inversion, *Geophys. J. R. astr. Soc.,* **57**(1), 137–157.

Jault, D., 2008. Axial invariance of rapidly varying diffusionless motions in the Earth's core interior, *Phys. Earth planet. Int.,* **166**(1–2), 67–76.

Jault, D., Gire, C. & Le Mouël, J.-L., 1988. Westward drift, core motions and exchanges of angular momentum between core and mantle, *Nature,* **333**(6171), 353–356.

Kalnay, E., 2003. *Atmospheric Modeling, Data Assimilation, and Predictability,* Cambridge University Press, Cambridge.

Korte, M. & Constable, C.G., 2005. Continuous geomagnetic field models for the past 7 millennia: 2. CALS7K, *Geochem., Geophys., Geosyst.,* **6,** Q02H16, doi:10.1029/2004GC000801.

Kuang, W., Tangborn, A., Jiang, W., Liu, D., Sun, Z., Bloxham, J. & Wei, Z., 2008. MoSST-DAS: the first generation geomagnetic data assimilation framework, *Commun. Comput. Phys.,* **3,** 85–108.

Kuang, W., Tangborn, A., Wei, Z. & Sabaka, T., 2009. Constraining a numerical geodynamo model with 100-years of geomagnetic observations, *Geophys. J. Int.,* **179**(3), 1458–1468.

Le Mouël, J.L., 1984. Outer core geostrophic flow and secular variation of Earth's magnetic field, *Nature,* **311,** 734–735.

Lesur, V., Wardinski, I., Asari, S., Minchev, B. & Mandea, M., 2010. Modelling the Earth's core magnetic field under flow constraints, *Earth, Planets, Space,* **62**(6), 503–516.

Lhuillier, F., Fournier, A., Aubert, J. & Hulot, G., 2011. The secular-variation timescale in geomagnetic field and dynamo models, *Geophys. Res. Lett.,* doi:10.1029/2011GL047356, in press.

Liu, D., Tangborn, A. & Kuang, W., 2007. Observing system simulation experiments in geomagnetic data assimilation, *J. geophys. Res.,* **112,** B08103, doi:10.1029/2006JB004691.

Lorenc, A.C., 1986. Analysis methods for numerical weather prediction, *Q. J. R. Meteorol. Soc.,* **112**(474), 1177–1194.

Lowes, F.J., 1974. Spatial power spectrum of the main geomagnetic field, and extrapolation to the core, *Geophys. J. R. astr. Soc.,* **36**(3), 717–730.

Mauersberger, P., 1956. Das Mittel der Energiedichte des geomagnetischen Hauptfeldes an der Erdoberfläche und seine säkulare Änderung, *Gerlands Beitr. Geophys,* **65,** 207–215.

Olsen, N., Mandea, M., Sabaka, T. & Tøffner-Clausen, L., 2009. CHAOS-2–a geomagnetic field model derived from one decade of continuous satellite data, *Geophys. J. Int.,* **179**(3), 1477–1487.

Pais, M.A. & Jault, D., 2008. Quasi-geostrophic flows responsible for the secular variation of the Earth's magnetic field, *Geophys. J. Int.,* **173**(2), 421–443.

Pais, M.A., Oliveira, O. & Nogueira, F., 2004. Nonuniqueness of inverted core-mantle boundary flows and deviations from tangential geostrophy, *J. geophys. Res.,* **109,** B08105, doi:10.1029/2004JB003012.

Rau, S., Christensen, U., Jackson, A. & Wicht, J., 2000. Core flow inversion tested with numerical dynamo models, *Geophys. J. Int.,* **141**(2), 485–497.

Reigber, C., Lühr, H. & Schwintzer, P., 2002. CHAMP mission status, *Adv. Space Res.,* **30**(2), 129–134.

Roberts, P.H. & Scott, S., 1965. On analysis of the secular variation, *J. Geomagnet. Geoelectr.,* **17**(2), 137–151.

Sakuraba, A., 2010. Numerical simulations of low-viscosity Earth-type dynamos, in *Proceedings of the 12th General Assembly of the SEDI*, Santa Barbara, CA.

Sakuraba, A. & Roberts, P.H., 2009. Generation of a strong magnetic field using uniform heat flux at the surface of the core, *Nat. Geosci.,* **2,** 802–805.

Thébault, E., Chulliat, A., Maus, S., Hulot, G., Langlais, B., Chambodut, A. & Menvielle, M., 2010. IGRF candidate models at times of rapid changes in core field acceleration, *Earth, Planets, Space,* **62**(10), 753–763, doi:10.5047/eps.2010.05.004.

Voorhies, C.V., 1986. Steady flows at the top of Earth's core derived from geomagnetic field models, *J. geophys. Res.,* **91,** 12 444–12 466.

Wessel, P. & Smith, W.H.F., 1991. Free software helps map and display data, *EOS, Trans. Am. geophys. Un.,* **72,** 441–445.

Whaler, K.A., 1986. Geomagnetic evidence for fluid upwelling at the core-mantle boundary, *Geophys. J. R. astr. Soc.,* **86**(2), 563–588.

Wicht, J. & Christensen, U.R., 2010. Torsional oscillations in dynamo simulations, *Geophys. J. Int.,* **181**(3), 1367–1380.

Wicht, J., Stellmach, S. & Harder, H., 2010. Numerical dynamo simulations: from basic concepts to realistic models, in *Handbook of Geomathematics,* pp. 459–502, eds Freeden, W., Nashed, M.Z. & Sonar, T., Springer, Berlin, doi:10.1007/978-3-642-01546-5_16.

Wunsch, C., 2006. *Discrete Inverse and State Estimation Problems,* Cambridge University Press, Cambridge.

APPENDIX A: DERIVATION OF THE KALMAN GAIN FORMULA

For the sake of completeness, we briefly demonstrate in this appendix the equivalence of eqs (13) and (12). The successive steps are the following: Start by writing

$$\mathbf{H}^\dagger = \mathbf{H}^\dagger, \tag{A1}$$

and add $\mathbf{H}^\dagger\mathbf{R}^{-1}\,\mathbf{H}\,\mathbf{P}^{\mathrm{b}}\,\mathbf{H}^\dagger$ on either side of the equal sign:

$$\mathbf{H}^\dagger\mathbf{R}^{-1}\mathbf{H}\mathbf{P}^{\mathrm{b}}\mathbf{H}^\dagger + \mathbf{H}^\dagger = \mathbf{H}^\dagger + \mathbf{H}^\dagger\mathbf{R}^{-1}\mathbf{H}\mathbf{P}^{\mathrm{b}}\mathbf{H}^\dagger. \tag{A2}$$

Factorize the left-hand and right-hand sides like so

$$\mathbf{H}^\dagger\mathbf{R}^{-1}[\mathbf{H}\mathbf{P}^{\mathrm{b}}\mathbf{H}^\dagger + \mathbf{R}] = [\mathbf{P}^{\mathrm{b}\,-1} + \mathbf{H}^\dagger\mathbf{R}^{-1}\mathbf{H}]\mathbf{P}^{\mathrm{b}}\mathbf{H}^\dagger. \tag{A3}$$

Now left-multiply either side of the equality by the inverse of $\mathbf{P}^{\mathrm{b}-1} + \mathbf{H}^\dagger\mathbf{R}^{-1}\,\mathbf{H}$ and right-multiply either side of the equality by the inverse of $\mathbf{H}\,\mathbf{P}^{\mathrm{b}}\,\mathbf{H}^\dagger + \mathbf{R}$. This procedure yields

$$[\mathbf{P}^{\mathrm{b}\,-1} + \mathbf{H}^\dagger\mathbf{R}^{-1}\mathbf{H}]^{-1}\mathbf{H}^\dagger\mathbf{R}^{-1} = \mathbf{P}^{\mathrm{b}}\mathbf{H}^\dagger[\mathbf{H}\mathbf{P}^{\mathrm{b}}\mathbf{H} + \mathbf{R}]^{-1}, \tag{A4}$$

which demonstrates the equivalence of the two formulas.

APPENDIX B: DESCRIPTION OF THE NUMERICAL MODEL OF THE GEODYNAMO

This appendix is geared towards readers willing to learn basic facts about our numerical model.

B1 Governing equations

Our 3-D numerical dynamo model discretizes the equations for the conservation of mass, momentum, and energy, together with the induction equation, in a rotating spherical shell of inner radius $b = 1220$ km and outer radius $c = 3485$ km. These equations are written in the framework of the modified Boussinesq approximation of Braginsky & Roberts (1995); the density anomaly which drives convective motion can have a chemical and/or a thermal origin, and it is described by the so-called codensity field C, which writes

$$C = \alpha\rho T' + \Delta\rho\xi', \tag{B1}$$

where α is the coefficient of thermal expansion, ρ is density, $\Delta\rho$ is the density difference between the light elements which contribute to convection and pure iron, and T' and ξ' are the local temperature and light element mass fraction departures from an isentropic, well-mixed, reference state.

Our model solves accordingly

$$\boldsymbol{\nabla} \cdot \boldsymbol{u} = 0, \tag{B2}$$

$$\rho \left(\partial_t \boldsymbol{u} + \boldsymbol{u} \cdot \boldsymbol{\nabla} \boldsymbol{u} + 2\boldsymbol{\Omega} \times \boldsymbol{u}\right) = -\boldsymbol{\nabla} \Pi + \boldsymbol{j} \times \boldsymbol{B} + \rho \nu \nabla^2 \boldsymbol{u} + C\boldsymbol{g}, \tag{B3}$$

$$\partial_t C + \boldsymbol{u} \cdot \boldsymbol{\nabla} C = \kappa \nabla^2 C + S_{T/\xi}, \tag{B4}$$

$$\partial_t \boldsymbol{B} = \boldsymbol{\nabla} \times (\boldsymbol{u} \times \boldsymbol{B}) + (1/\mu\sigma)\nabla^2 \boldsymbol{B}, \tag{B5}$$

where $\boldsymbol{u}$ is velocity, $\boldsymbol{\Omega}$ is the angular velocity of the Earth, Π is the modified pressure, $\boldsymbol{j}$ is the electric current density, ν is the kinematic viscosity, κ is the thermal-chemical diffusivity, $S_{T/\xi}$ is a volumetric density source/sink term, equal to F/V, where F is the (positive) total mass anomaly flux, and V is the volume of the core (Aubert *et al.* 2009), μ is the magnetic permeability, and σ is the electrical conductivity. This set of equations is supplemented with no-slip boundary conditions for velocity, insulating magnetic boundary conditions at the inner-core boundary (ICB) and at the CMB, a prescribed codensity at the ICB and a null codensity flux $\boldsymbol{\nabla} C = \boldsymbol{0}$ at the CMB. A proper set of initial conditions is also necessary to start the dynamo. Following the prescription of these initial conditions, the first stage of a model run is characterized by a transient behaviour; the sequence we shall consider in the following starts after the effective completion of that transient.

In dynamo modelling, the numerical price to pay to prescribe its Earth-like value to every single external or physical control parameter entering the set of equations written above is simply out of reach. The particular model we choose makes no exception, as we shall see below.

B2 Non-dimensional parameters

Numerical dynamo models operate practically in a non-dimensional world whose relevance follows from the principles of dimensional analysis and self-similarity (e.g. Barenblatt 1996). Π-theorem applied to the set of equations written above indicates that four non-dimensional parameters suffice to characterize the system. The definition of these four non-dimensional parameters (which combine the physical properties of the fluid and other external parameters) depends ultimately on the various scales chosen to describe the system. Regarding the PARODY-JA code we employ, the choice of scales is summarized in Aubert *et al.* (2009). This choice implies in turn to resort to the following four non-dimensional numbers: the Ekman number E, Prandtl number Pr, magnetic Prandtl number Pm, and Rayleigh number Ra, defined respectively as

$$\mathrm{E} = \frac{\nu}{\Omega \mathcal{L}^2}, \tag{B6}$$

$$\mathrm{Pr} = \frac{\nu}{\kappa}, \tag{B7}$$

$$\mathrm{Pm} = \nu\mu\sigma, \tag{B8}$$

and

$$\mathrm{Ra} = \frac{g_0 F}{4\pi\rho\Omega^3\mathcal{L}^4}. \tag{B9}$$

In these expressions, $\mathcal{L}$ is the length scale (the depth $c - b = 2265$ km), $\Omega = \|\boldsymbol{\Omega}\|$, and g_0 is the acceleration of gravity at $r = c$. The model we choose has

$$(\mathrm{E}, \mathrm{Pr}, \mathrm{Pm}, \mathrm{Ra}) = (10^{-3}, 1, 4, 5.8\ 10^{-3}), \tag{B10}$$

to compare with the approximate values for the Earth:

$$(\mathrm{E}, \mathrm{Pr}, \mathrm{Pm}, \mathrm{Ra}) \approx (10^{-14}, 10^{-2}, 10^{-5}, 10^{-13}). \tag{B11}$$

These numbers are partly based on estimates of the physical properties of iron under core conditions (for the first three), and on estimates based on scaling laws for the last one (Christensen & Aubert 2006; Aubert *et al.* 2009). Note in particular that the large value of Pm is necessary for dynamo action to be possible in our (very viscous) working fluid. Even if these four input parameters alone suffice to describe the model uniquely and please the self-similarity zealot, it is possible to characterize the magneto-hydrodynamic behaviour of the model by introducing extra non-dimensional output numbers (based on diagnostics, like rms quantities averaged over the model integration time T). A well-known and useful example is the magnetic Reynolds number Rm given by

$$\mathrm{Rm} = \frac{U_{\mathrm{rms}}\mu\sigma}{\mathcal{L}}, \tag{B12}$$

which happens to be 100 in the model chosen for this study (U_{rms} is the rms velocity). Rm is related to the hydrodynamic Reynolds number Re via

$$\mathrm{Rm} = \mathrm{PmRe}. \tag{B13}$$

Again, having a large enough value of Pm allows Rm to exceed its critical value, in spite of the smallness of Re.